To be submitted to the Astrophysical Journal
Preprint typeset using LaTeX style emulateapj v. 5/2/11

arXiv:1701.02151v1 [astro-ph.CO] 9 Jan 2017

MICROLENSING CONSTRAINTS ON $10^{-10}M_{\odot}$-SCALE PRIMORDIAL BLACK HOLES FROM HIGH-CADENCE OBSERVATION OF M31 WITH HYPER SUPRIME-CAM

Hiroko Niikura[1,2], Masahiro Takada[1], Naoki Yasuda[1], Robert H. Lupton[3], Takahiro Sumi[4], Surhud More[1], Anupreeta More[1], Masamune Oguri[1,2,5], Masashi Chiba[6]

To be submitted to the Astrophysical Journal

ABSTRACT

We use the Subaru Hyper Suprime-Cam (HSC) to conduct a high-cadence (2 min sampling) 7 hour long observation of the Andromeda galaxy (M31) to search for the microlensing magnification of stars in M31 due to intervening primordial black holes (PBHs) in the halo regions of the Milky Way (MW) and M31. The combination of an aperture of 8.2m, a field-of-view of 1.5 degree diameter, and excellent image quality ($\sim 0.6''$) yields an ideal dataset for the microlensing search. If PBHs in the mass range $M_{\rm PBH} = [10^{-13}, 10^{-6}]M_{\odot}$ make up a dominant contribution to dark matter (DM), the microlensing optical depth for a *single* star in M31 is $\tau \sim 10^{-4}$–10^{-7}, owing to the enormous volume and large mass content between M31 and the Earth. The HSC observation allows us to monitor more than tens of millions of stars in M31 and in this scenario we should find many microlensing events. To test this hypothesis, we extensively use an image subtraction method to efficiently identify candidate variable objects, and then monitor the light curve of each candidate with the high cadence data. Although we successfully identify a number of real variable stars such as eclipse/contact binaries and stellar flares, we find only one possible candidate of PBH microlensing whose genuine nature is yet to be confirmed. We then use this result to derive the most stringent upper bounds on the abundance of PBHs in the mass range. When combined with other observational constraints, our constraint rules out almost all the mass scales for the PBH DM scenario where all PBHs share a single mass scale.

Subject headings: dark matter – gravitational lensing: micro – stars: black holes

1. INTRODUCTION

The nature of dark matter (DM) remains hotly studied and debated both theoretically and observationally, and is one of the most important problems in cosmology. Previous studies have suggested that DM is non-baryonic, non-relativistic, and interacts with ordinary matter only via gravity (Zwicky 1937; Rubin et al. 1978; Davis et al. 1985; Clowe et al. 2006; Dodelson & Liguori 2006). Currently, unknown stable particle(s) beyond the Standard Model of Particle Physics, so-called Weakly Interacting Massive Particles (WIMPs), are considered as viable candidates (e.g. Jungman et al. 1996). However they have yet to be detected in either elastic scattering experiments or in collider experiments (e.g., Klasen et al. 2015). Primordial black holes (PBH), first proposed by Zel'dovich & Novikov (1967) (also see Hawking 1971; Carr & Hawking 1974; Carr 1975), are also viable candidates for DM. PBHs can be formed by the gravitational collapse of the Hubble patch in the radiation dominated era of the Universe if a large overdensity of $\delta \sim O(0.1)$ is injected into the patch. It is also advocated that PBHs can be progenitors of binary black holes (Sasaki et al. 2016; Bird et al. 2016; Kawasaki et al. 2016b; Inomata et al. 2016) that are gravitational wave sources, recently detected by the LIGO-Virgo collaboration (Abbott et al. 2016). The abundance of PBHs at different mass scales is constrained by various observations except for a mass window of 10^{21}–10^{24} g corresponding to 10^{-12}–$10^{-9}M_{\odot}$ (see Carr et al. 2016, for a recent review). Thus it is of critical importance to further explore observational constraints on the PBH abundance for this mass window.

Gravitational microlensing has been used as a powerful method to probe DM in the Milky Way (MW) since the theoretical proposal in Paczynski (1986) (also see Griest et al. 1991; Roulet & Mollerach 1997; Wambsganss 2006). Microlensing can be detected through the time-variable magnification of a background star when the lensing object and the background star move relative to each other on the sky. Although massive compact halo objects (MACHOs) such as brown dwarfs are some of the most secure baryonic candidates that behave like DM, the MACHO and EROS experiments ruled out the scenario that MACHOs of $[10^{-9}, 10]M_{\odot}$ mass scales are a majority component of DM, because these experiments did not find a sufficient number of the MACHO microlensing events of stars in the Large Magellanic Cloud (LMC) (Alcock et al. 2000; Bennett 2005; Tisserand et al. 2007; Wyrzykowski et al. 2010). Recently Griest et al. (2014) (also see Griest et al. 2011) used the public 2-years Kepler data to search for the microlensing events from $\sim 10^5$ stars in an open cluster at a distance of about 4 kpc and derived new upper limits on the abundance of PBHs of $10^{-8}M_{\odot}$ mass scale. However, the Kepler data primarily has a cadence of 30 min and the number of source stars ($\sim 10^5$) is relatively small compared to the microlensing optical depth ($\tau \sim 10^{-7}$).

With the aim of constraining the abundance of PBH with mass scales $10^{-10}M_{\odot}$, we have carried out a high cadence observation of the Andromeda galaxy (M31), with the Subaru

[1] Kavli Institute for the Physics and Mathematics of the Universe (WPI), The University of Tokyo Institutes for Advanced Study (UTIAS), The University of Tokyo, Chiba, 277-8583, Japan
[2] Physics Department, The University of Tokyo, Bunkyo, Tokyo 113-0031, Japan
[3] Department of Astrophysical Sciences, Princeton University, Peyton Hall, Princeton NJ 08544 USA
[4] Department of Earth and Space Science, Graduate School of Science, Osaka University, Toyonaka, Osaka 560-0043, Japan
[5] Research Center for the Early Universe, University of Tokyo, Tokyo 113-0033, Japan
[6] Astronomical Institute, Tohoku University, Aoba-ku, Sendai 980-8578, Japan

Hyper Suprime-Cam (HSC), in order to search for microlensing events of M31 stars by intervening PBHs in both the halo regions of MW and M31. M31 is the largest spiral galaxy, nearest to the MW, at a distance of about 770 kpc (the distance modulus $\mu \simeq 24.4$ mag). Even a single night of HSC/Subaru data yields an ideal dataset to search for the PBH microlensing events. First, the 1.5 degree diameter field-of-view of HSC (Miyazaki et al. 2015) allows us to cover the entire region of M31 covering both the bulge, disk and halo regions. The 8.2m large aperture and its superb image quality (0.6″ seeing) allow us to detect fluxes from main sequence stars in M31, even with short exposure, here 90 sec exposure, because we can reach to about 26 mag depth. This allows us to monitor a sufficiently large number of stars in M31 simultaneously. Secondly, the 90 sec short exposure and a short ∼35 sec readout time enable us to take data at an unprecedented cadence of 2 min, which allows us to search for PBHs of smaller mass scales than done in Griest et al. (2014). Thirdly, there is a huge volume between M31 and the Earth, leading to a large optical depth of PBH microlensing to each star in M31 as we will show; $\tau \sim 10^{-7}$–10^{-4} for PBHs in the mass range of $M_{\rm PBH} \simeq [10^{-13}, 10^{-6}]M_\odot$, if PBHs constitute a majority of DM in the MW and M31 halos. Hence, by monitoring more than ten million stars in M31, we should be able to find many events of the PBH microlensing if PBHs exist.

However, the analysis of the observations is quite challenging. Since M31 is a dense star field and the counts in each CCD pixel can be from multiple stars, we are in the regime of having to deal with the microlensing effect on unresolved stars, i.e., pixel lensing (Crotts 1992; Baillon et al. 1993; Gould 1996) (also see Calchi Novati 2010, for a review). This is one of the main reasons that the previous observational efforts for the microlensing search towards M31 have been unsuccessful (Crotts & Tomaney 1996; Calchi Novati et al. 2005; de Jong et al. 2006; Riffeser et al. 2008; Calchi Novati et al. 2009; Lee et al. 2012; Calchi Novati et al. 2014, and also see references therein). Another reason for the unsuccessful result is that the previous works used data from smaller aperture telescopes, and the quality of the data is not as good as our HSC/Subaru data. To tackle the pixel lensing problem, we will heavily use the image subtraction technique described in Alard & Lupton (1998), which is fully integrated in the HSC pipeline (Bosch et al. in preparation). By subtracting the reference image from the target image, we can efficiently identify variable star candidates that pop up in the difference image. Then by repeating the image subtraction for different images for multiple visits (188 visits for our case), we can measure the light curve of each candidate, which allows us to efficiently search for microlensing candidates. In fact our analysis finds many secure candidates of variable stars such as stellar flares and binary systems.

The structure of this paper is as follows. In Section 2, after a brief review of the microlensing phenomena, we first derive an event rate for microlensing due to the intervening PBHs for a single star in M31, by employing a halo model for the MW and M31. In Section 3 we describe the details of our data analysis including the image subtraction technique, and define the master catalog of variable star candidates. In Section 4 we describe the selection criteria for microlensing events from the catalog of variable star candidates. In Section 5, we use the result to derive an experimental upper bound on the abundance of PBHs as a function of PBH mass. We then discuss how different assumptions in our analysis affect the upper bound in Section 6 and present our conclusions and summary in Section 7.

2. EVENT RATE OF PBH MICROLENSING FOR M31 STARS

In this section we estimate event rates of PBH microlensing for a star in M31. We extend the formulation in previous studies (Griest et al. 1991; Alcock et al. 1996; Kerins et al. 2001; Riffeser et al. 2006) to microlensing cases due to PBHs in the halo regions of MW and M31 for a source star in M31.

2.1. *Microlensing basics*

If a star in M31[7] and a foreground PBH are almost perfectly aligned along the line-of-sight to an observer, the star is multiply imaged due to strong gravitational lensing. In case these multiple images are unresolved, the flux from the star appears magnified. When the source star and the lensing PBH are separated by an angle β on the sky, the total lensing magnification, i.e. the sum of the magnification of the two images, is

$$A = A_1 + A_2 = \frac{u^2+2}{u\sqrt{u^2+4}}, \tag{1}$$

where $u \equiv (d \times \beta)/R_E$, and d is the distance to a lensing PBH. The Einstein radius R_E is defined as

$$R_E^2 = \frac{4GM_{\rm PBH}D}{c^2}, \tag{2}$$

where $M_{\rm PBH}$ is the PBH mass. D is the lensing weighted distance, $D \equiv d(1-d/d_{\rm s})$, where $d_{\rm s}$ is the distance to a source star in M31, and d is the distance to the PBH. By plugging typical values of the parameters, we can find the typical Einstein radius:

$$\theta_E \equiv \frac{R_E}{d} \simeq 3\times10^{-8}\ {\rm arcsec}\left(\frac{M_{\rm PBH}}{10^{-8}M_\odot}\right)^{1/2}\left(\frac{d}{100\ {\rm kpc}}\right)^{-1/2} \tag{3}$$

where we assumed $d_{\rm s} = 770$ kpc for distance to a star in M31 and we assumed $D \sim d$ for simplicity, and employed $M_{\rm PBH} = 10^{-8}M_\odot$ as a working example for the sake of comparison with Griest et al. (2014). In the following analysis we will consider a wide range of PBH mass scales. The PBH lensing phenomena we search for are in the microlensing regime; we cannot resolve two lensed images with angular resolution of an optical telescope, and we can measure only the total magnification. A size of a star in M31 is viewed as

$$\theta_s \simeq \frac{R_s}{d_{\rm s}} \simeq 5.8\times10^{-9}\ {\rm arcsec}\ , \tag{4}$$

if the source star has a similar size to the solar radius ($R_\odot \simeq 6.96\times10^{10}$ cm). Comparing with Eq. (3) we find that the Einstein radius becomes smaller than the source size if PBH mass $M_{\rm PBH} \lesssim 10^{-10}M_\odot$ corresponding to $M_{\rm PBH} \lesssim 10^{23}$ g. We discuss such lighter PBHs in Section 6, where we will take into account the effect of finite source size on the microlensing (Witt & Mao 1994; Cieplak & Griest 2013; Griest et al. 2014).

Since the PBH and the source star move relative to each other on the sky, the lensing magnification varies with time, allowing us to identify the star as a variable source in a difference image from the cadence observation. The microlensing

[7] Throughout this paper we assume that a source star is in M31, not in the MW halo region, because of the higher number density on the sky.

light curve has a characteristic timescale that is needed for a lensing PBH to move across the Einstein radius:

$$t_E \equiv \frac{R_E}{v}, \tag{5}$$

where v is the relative velocity. Assuming fiducial values for these parameters, we can estimate the typical timescale as

$$t_E \simeq 34 \min \left(\frac{M_{\rm PBH}}{10^{-8} M_\odot}\right)^{1/2} \left(\frac{d}{100\ {\rm kpc}}\right)^{-1/2} \left(\frac{v}{200\ {\rm km/s}}\right)^{-1}, \tag{6}$$

where we assumed $v = 200$ km/s for the typical relative velocity. Thus the microlensing light curve is expected to vary over several tens of minutes, and should be well sampled by our HSC observation. It should also be noted that a PBH closer to the Earth gives a longer timescale light curve for a fixed velocity. Since we can safely assume that the relative velocity stays constant during the Einstein radius crossing, the light curve should have a symmetric shape around the peak, which we will use to eliminate fake candidates.

2.2. *Microlensing event rate*

Here we estimate expected microlensing event rates from PBHs assuming that they consist of a significant fraction of DM in the MW and M31 halo regions.

We first need to assume a model for the spatial distribution of DM (therefore PBHs) between M31 and us (the Earth). Here we simply assume that the DM distribution in each halo region of MW or M31 follows the NFW profile (Navarro et al. 1997):

$$\rho_{\rm NFW}(r) = \frac{\rho_c}{(r/r_s)(1 + r/r_s)^2}, \tag{7}$$

where r is the radius from the MW center or the M31 center, r_s is the scale radius and ρ_c is the central density parameter. In this paper we adopt the halo model in Klypin et al. (2002): $M_{\rm vir} = 10^{12} M_\odot$, $\rho_c = 4.88 \times 10^6\ M_\odot/{\rm kpc}^3$, and $r_s = 21.5$ kpc for MW, taken from Table 2 in the paper, while $M_{\rm vir} = 1.6 \times 10^{12} M_\odot$, $\rho_c = 4.96 \times 10^6\ M_\odot/{\rm kpc}^3$, and $r_s = 25$ kpc for M31, taken from Table 3. Thus we assume a slightly larger DM content for the M31 halo than the MW halo. Dark matter profiles with these parameters have been shown to fairly well reproduce the observed rotation curves for MW and M31, respectively. There might be an extra DM contribution in the intervening space between MW and M31, e.g. due to a filamentary structure bridging MW and M31. However, we do not consider such an unknown contribution.

Consider a PBH at a distance d (kpc) from the Earth and in the angular direction to M31, $(l, b) = (121.2°, -21.6°)$ in the Galactic coordinate system. Assuming that the Earth is placed at distance $R_\oplus = 8.5$ kpc from the MW center, we can express the separation to the PBH from the MW center, $r_{\rm MW-PBH}$, in terms of the distance from the Earth, d, as

$$r_{\rm MW-PBH}(d) = \sqrt{R_\oplus^2 - 2R_\oplus d \cos(l)\cos(b) + d^2}. \tag{8}$$

If we ignore the angular extent of M31 on the sky (which is restricted to 1.5 degree in diameter for our study), the distance to the PBH from the M31 center, $r_{\rm M31-PBH}$, is approximately given by,

$$r_{\rm M31-PBH}(d) \simeq d_{\rm s} - d, \tag{9}$$

where we approximated the distance to a source star in M31 to be the same as the distance to the center of M31, $D_{\rm M31} \simeq d_{\rm s}$, which we assume to be equal to $d_{\rm s} = 770$ kpc throughout this paper.

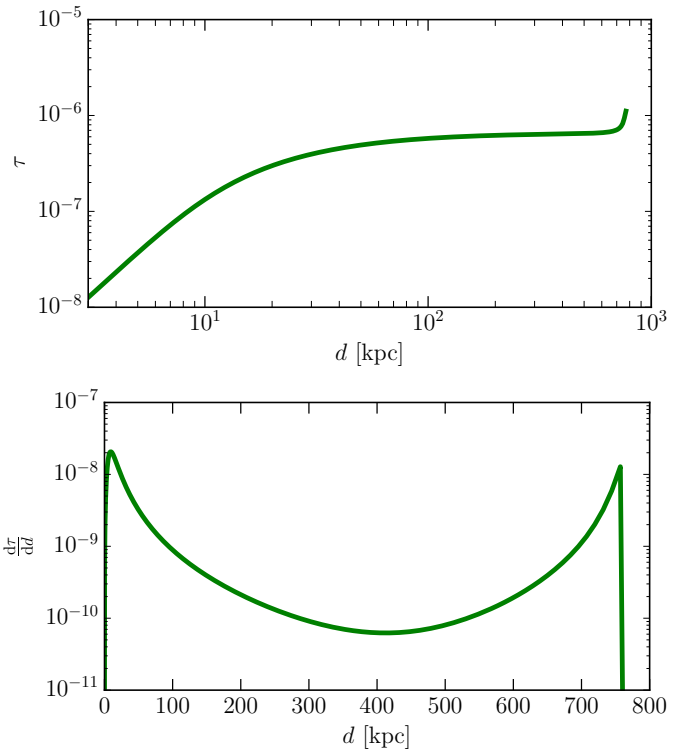

Figure 1. *Upper*: The optical depth of PBH microlensing effect on a single star in M31 as a function of the distance to PBH, d, which can be obtained by integrating the integrand in Eq. (10) over $[0, d]$, rather than $[0, d_{\rm s}]$. The optical depth is independent of PBH mass, and we assumed NFW parameters to model the DM distribution in each of the MW and M31 halo regions, where we determined the NFW parameters so as to reproduce their rotation curves (see text for details). *Lower*: Similar plot, but the fractional contribution of PBHs at the distance, d, to the optical depth. Note that d in the x-axis is in linear scale. The area under this curve up to d gives the optical depth to d in the upper plot.

By using Eqs. (7)-(9), we can compute the DM density, contributed from both the MW and M31 halos, as a function of the distance to PBH, d.

Assuming that PBHs make us the DM content by a a fraction, $\Omega_{\rm PBH}/\Omega_{\rm DM}$, we can compute the optical depth τ for the microlensing of PBHs with mass $M_{\rm PBH}$ for a *single* star in M31. The optical depth is defined as the probability for a source star to be inside the Einstein radius of a foreground PBH on the sky or equivalently the probability for the magnification of source flux to be greater than that at the Einstein radius, $A \geq 1.34$ (Paczynski 1986):

$$\tau = \frac{\Omega_{\rm PBH}}{\Omega_{\rm DM}} \int_0^{d_{\rm s}} {\rm d}d\, \frac{\rho_{\rm DM}(d)}{M_{\rm PBH}} \pi R_E^2(d, M_{\rm PBH}). \tag{10}$$

Here the mass density field of DM is given by the sum of NFW profiles for the MW and M31 halos: $\rho_{\rm DM}(d) = \rho_{\rm NFW,MW}(d) + \rho_{\rm NFW,M31}(d)$. Note that, because of $R_E^2 \propto M_{\rm PBH}$, the optical depth is independent of PBH mass.

In Fig. 1, we show the optical depth of PBH microlensing for a single star in M31, calculated using the above equation. Here we have assumed that all the DM in the halo regions of MW and M31 is composed of PBHs, i.e., $\Omega_{\rm PBH}/\Omega_{\rm DM} = 1$. The optical depth for microlensing, $\tau \sim 10^{-6}$, is larger compared to that to LMC or a star cluster in MW ($\tau \sim 10^{-7}$) by an order of magnitude, due to the enormous volume and

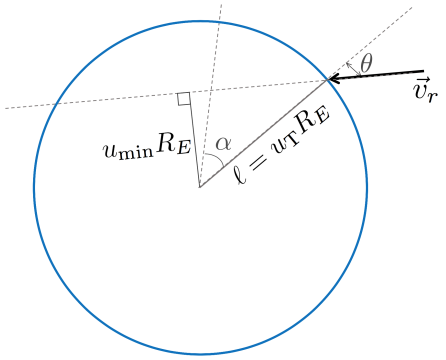

Figure 2. A schematic illustration of configurations of a lensing PBH and a source star in M31 in the lens plane, following Fig. 4 of Griest et al. (1991). The orbit of a lensing PBH, around a source star in M31 (placed at the origin in this figure), is parameterized as in the figure, which is used to derive the microlensing event rate (see text for details).

large mass content between the Earth and M31. The PBHs in each of the MW and M31 halos result in a roughly equal contribution to the optical depth to an M31 star. Although there is an uncertainty in the DM density in the inner region of MW or M31 (at radii $\lesssim 10$ kpc) due to poorly-understood baryonic effects, the contribution is not large.

Next we estimate the rate for microlensing events with a given timescale for its light curve. First we model the velocity distribution of DM in the halo regions. We simply assume an isotropic Maxwellian velocity distribution for DM particles (e.g. Jungman et al. 1996):

$$f(\mathbf{v};r)\mathrm{d}^3\mathbf{v} = \frac{1}{\pi^{3/2}v_{\rm c}(r)^3}\exp\left[-\frac{|\mathbf{v}|^2}{v_{\rm c}(r)^2}\right]\mathrm{d}^3\mathbf{v} \tag{11}$$

where $V_{\rm halo}(r)$ is the velocity dispersion at radius r from the MW or M31 center. For $V_{\rm halo}(r)$, we assume that it is given as

$$v_{\rm c}(r) = \sqrt{\frac{GM_{\rm NFW}(<r)}{r}}, \tag{12}$$

where $M_{\rm NFW}(<r)$ is the interior mass within radius r from the halo center, defined as $M_{\rm NFW}(<r) = 4\pi\rho_s r_s^3[\ln(1+c) - c/(1+c)]$, where $c = r/r_s$ for each of the MW and M31 halos.

We start from the geometry and variables shown in Fig. 4 of Griest et al. (1991) and their Eq. (10) (see Fig. 2), which gives the rate $\mathrm{d}\Gamma$ of PBHs entering a volume element along the line-of-sight where they can cause microlensing for a single star in M31:

$$\mathrm{d}\Gamma = \frac{\Omega_{\rm PBH}}{\Omega_{\rm DM}}\frac{\rho_{\rm DM}(d)}{M_{\rm PBH}}\frac{u_{\rm T}R_{\rm E}}{\pi v_{\rm c}^2}\exp\left[-\frac{v_{\rm r}^2}{v_{\rm c}^2}\right]v_{\rm r}^2\cos\theta\,\mathrm{d}v_{\rm r}\,\mathrm{d}\theta\,\mathrm{d}d\,\mathrm{d}\alpha. \tag{13}$$

Here $n_{\rm PBH}(d)$ is the number density of PBHs at the distance d from the Earth, $v_{\rm r}$ is the velocity of the PBH in the lens plane, θ is the angle at which the PBH enters the volume element, and α is an angle with respect to an arbitrary direction in the lens plane, as shown in Fig. 2. Microlensing events are identified if they have a given threshold magnification $A_{\rm T}$ at peak. This threshold magnification defines a threshold impact parameter with respect to the Einstein radius of a PBH, $u_{\rm T} = R_{\rm T}/R_{\rm E}$. Compared to Griest et al. (1991), we have further ignored motions of source stars for simplicity, i.e. $v_{\rm t} = 0$. The parameters vary in the range of $\theta \in [-\pi/2, \pi/2]$, $\alpha \in [0, 2\pi]$, $v_{\rm r} = [0, \infty)$.

The time scale for the microlensing event described by the above geometry is given by $\hat{t} = 2R_{\rm E}\cos\theta\, u_{\rm T}/v_{\rm r}$. Thus the differential rate of microlensing events, occurring per unit time scale $\hat{t}$, is given by

$$\frac{\mathrm{d}\Gamma}{\mathrm{d}\hat{t}} = \frac{\Omega_{\rm PBH}}{\Omega_{\rm DM}}\int_0^{d_{\rm s}}\mathrm{d}d\int_0^{\infty}\mathrm{d}v_{\rm r}\int_{-\pi/2}^{\pi/2}\mathrm{d}\theta\int_0^{2\pi}\mathrm{d}\alpha\,\frac{\rho_{\rm DM}(d)}{M_{\rm PBH}} \times\frac{u_{\rm T}R_{\rm E}}{\pi v_{\rm c}^2}\exp\left[-\frac{v_{\rm r}^2}{v_{\rm c}^2}\right]v_{\rm r}^2\cos\theta\;\delta_{\rm D}\left(\hat{t} - \frac{2R_{\rm E}u_{\rm T}\cos\theta}{v_{\rm r}}\right). \tag{14}$$

Using the Dirac-delta function identity,

$$\delta_{\rm D}\left(\hat{t} - \frac{2R_{\rm E}u_{\rm T}\cos\theta}{v_{\rm r}}\right) = \delta_{\rm D}\left(v_{\rm r} - \frac{2R_{\rm E}u_{\rm T}\cos\theta}{\hat{t}}\right)\frac{v_{\rm r}^2}{2R_{\rm E}u_{\rm T}\cos\theta}, \tag{15}$$

and integrating over α and $v_{\rm r}$, we obtain

$$\frac{\mathrm{d}\Gamma}{\mathrm{d}\hat{t}} = \frac{\Omega_{\rm PBH}}{\Omega_{\rm DM}}\int_0^{d_{\rm s}}\mathrm{d}d\int_{-\pi/2}^{\pi/2}\mathrm{d}\theta\,\frac{\rho_{\rm DM}(d)}{M_{\rm PBH}v_{\rm c}^2}v_{\rm r}^4\exp\left[-\frac{v_{\rm r}^2}{v_{\rm c}^2}\right], \tag{16}$$

with $v_{\rm r} = 2R_{\rm E}u_{\rm T}\cos\theta/\hat{t}$. One can rewrite this equation by changing variable θ to the minimum impact $u_{\rm min} = u_{\rm T}\sin\theta$, such that, $\mathrm{d}\theta = \mathrm{d}u_{\rm min}/\sqrt{u_{\rm T}^2 - u_{\rm min}^2}$. This results in

$$\frac{\mathrm{d}\Gamma}{\mathrm{d}\hat{t}} = 2\frac{\Omega_{\rm PBH}}{\Omega_{\rm DM}}\int_0^{d_{\rm s}}\mathrm{d}d\int_0^{u_T}\frac{\mathrm{d}u_{\rm min}}{\sqrt{u_{\rm T}^2 - u_{\rm min}^2}}\frac{\rho_{\rm DM}(d)}{M_{\rm PBH}v_{\rm c}^2}v_{\rm r}^4\exp\left[-\frac{v_{\rm r}^2}{v_{\rm c}^2}\right], \tag{17}$$

where $v_{\rm r} = 2R_E\sqrt{u_{\rm T}^2 - u_{\rm min}^2}/\hat{t}$. To compute the event rate due to PBHs in both the halo regions of MW and M31, we sum the contributions, $\mathrm{d}\Gamma = \mathrm{d}\Gamma_{\rm MW} + \mathrm{d}\Gamma_{\rm M31}$. As we described above, we can express the centric radius of each halo, r, entering into $v_{\rm c}(r)$, in terms of the distance to the lensing PBH, d; $r = r(d)$. Unless explicitly stated, we will employ $u_{\rm T} = 1$ as our default choice.

Fig. 3 shows the expected event rate for the PBH microlensing, computed using Eq. (17). Here we show the event rate as a function of the full-width-half-maximum (FWHM) timescale of the light curve, which matches our search of microlensing events from the real HSC data. If a PBH is in the mass range $M = [10^{-12}, 10^{-7}]M_\odot \simeq 2\times[10^{21}, 10^{26}]$ g, it causes the microlensing event that has a typical timescale in the range of $[10^{-1}, 1]$ hour. The lighter or heavier PBHs tend to cause a shorter or longer timescale event. The event rate is quite high up to 10^{-4} for a microlensing timescale with $[0.1, 1]$ hours. That is, if we take about 10 hours observation and observe 10^8 stars at once for each exposure, we expect many events up to 10^4 events (because $10^{-4}\times 10$ [hour] $\times$ 0.1 [hour] $\simeq 10^4$), assuming that such PBHs constitute a majority of DM in the intervening space bridging MW and M31. The right figure shows that the PBHs in the M31 halo region give a slightly larger contribution to the event rate, because we assumed a larger halo mass for M31 than that of MW. Thus the high-cadence HSC observation of M31 is suitable for searching for microlensing events of PBHs.

2.3. *Light Curve characterization in pixel lensing regime*

As we described above, the timescale for the PBH and M31 star microlensing system is typically several tens of minutes for a PBH with $10^{-8}M_\odot$. However, there is an observational challenge. Since the M31 region is such a dense star field, fluxes from multiple stars are overlapped in each CCD pixel (0.17″ pixel scale for HSC/Subaru). In other words individual

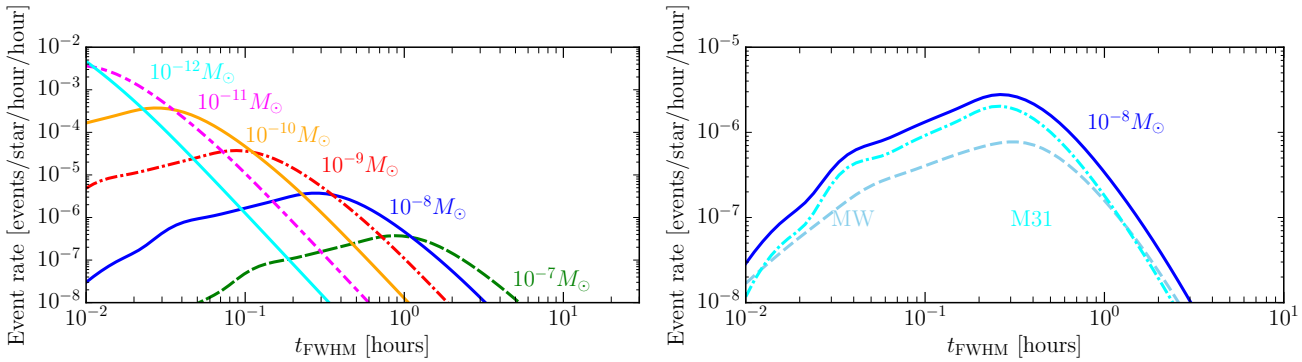

Figure 3. The differential event rate of PBH microlensing for a single M31 star (Eq. 17); the rate per unit observation time (hour), per a single source star in M31, and per unit timescale of the microlensing light curve (hour) for PBHs of a given mass scale. Here we assumed that all the DM in the MW and M31 halo regions is made of PBHs; $\Omega_{\rm PBH}/\Omega_{\rm DM} = 1$. The x-axis is the full-width-half-maximum (FWHM) timescale of microlensing light curve. The lighter or heavier PBH has a shorter or longer timescale of microlensing light curve. The right panel shows the relative contribution to the microlensing event rate due to PBHs in either MW or M31 halo region, for the case of $M_{\rm PBH} = 10^{-8}M_\odot$.

stars are not resolved even with the Subaru angular resolution (about 0.6″ for the seeing size). Hence we cannot identify which individual star in M31 is strongly lensed by a PBH, even if it occurs. Such a microlensing of unresolved stars falls in the "pixel microlensing" regime (Gould 1996) (also see Calchi Novati 2010, for a review).

To identify microlensing events in the pixel microlensing regime requires elaborate data reduction techniques. In this paper, we use the image subtraction or image difference technique first described in Alard & Lupton (1998). The image difference technique allows us to search for variable objects including candidate stars that undergo microlensing by PBHs. In brief, starting with the time sequenced $N_{\rm exp}$ images of M31, the analysis proceeds as follows. (i) We generate a reference image by co-adding some of the best-seeing images in order to gain a higher signal-to-noise. Next we subtract this reference image from each of the $N_{\rm exp}$ images after carefully matching their point spread functions (PSFs) as described in Alard & Lupton (1998). (ii) We search for candidate variable objects that show up in the difference image. In reality, if the image subtraction is imperfect, the difference image would contain many fake candidates, as we will discuss further. (iii) Once secure variable objects are detected, we determine the position (RA and dec) of each variable object in the difference image. We perform PSF photometry for each variable candidate using the PSF center to be at the position of the candidate in the difference image. By repeating the PSF photometry in each difference image of the $N_{\rm exp}$ images, we can measure the light curve of the candidate as a function of the observation time.

The light curve of a microlensing event obtained using the PSF flux in the difference image at time t, obtained as described above, can be expressed as

$$\Delta F(t) = F_0\,[A(t) - A(t_{\rm ref})]\,, \tag{18}$$

where $\Delta F(t)$ is the differential flux of the star at time t relative to the reference image, F_0 is the intrinsic flux, $A(t)$ is the lensing magnification at t and $A(t_{\rm ref})$ is the magnification at the time of the reference image, $t_{\rm ref}$. In the above equation, $\Delta F(t)$ is a direct observable, and others $(F_0, A(t), A(t_{\rm ref}))$ are parameters that have to be modeled.

As can be seen from Eq. (1), the light curve for the microlensing of a point source by a point mass can be characterized by two parameters. The first parameter is the maximum amplification $A_0 = A(u_{\rm min})$ when the lensing PBH is closest to a source star on the sky, where $u_{\rm min}$ is the impact parameter relative to the Einstein radius R_E ($u_{\rm min}$ is dimension-less). The second one is the timescale of the light curve, which depends on the Einstein radius as well as the transverse velocity of the PBH moving across the sky. For the timescale parameter we use the FWHM timescale of the microlensing light curve, $t_{\rm FWHM}$, instead of t_E, defined as

$$A\left(\frac{t_{\rm FWHM}}{2}\right) - 1 \equiv \frac{A_0 - 1}{2}. \tag{19}$$

Thus the light curve of microlensing can be fully modeled by the three parameters, F_0, $u_{\rm min}$ and $t_{\rm FWHM}$. In the following we will use the three parameters when performing a fitting of the microlensing model to the observed light curve of microlensing candidate in the image difference. Note that the use of $t_{\rm FWHM}$, instead of t_E, gives slightly less degenerate constraints on the parameters (Gondolo 1999).

3. DATA ANALYSIS AND OBJECT SELECTION

3.1. *Observations*

The HSC camera has 104 science detectors with a pixel scale of 0.17″ (Miyazaki et al. 2015). The 1.5 degree diameter FoV of HSC enables us to cover the entire region of M31, from the inner bulge to the outer disk and halo regions with a single pointing. The pointing is centered at the coordinates of the M31 central region: (RA, dec) = (00h 42m 44.420s,+41d 16m 10.1s). We do not perform any dithering between different exposures in order to compare stars in the same CCD chip, which makes the image difference somewhat easier. However, in reality the HSC/Subaru system has some subtle inaccuracies in its auto-guidance and/or pointing system. This results in variations in the pointings of different exposures, typical variations range from few to a few tens of pixels.

Fig. 4 shows the configuration of the 104 CCD chips relative to the image of M31 on the sky. The white-color boxes denote locations of HSC "patches", which are convenient tessellations of the HSC FoV. The image subtraction and the search of microlensing events will be done on a patch-by-patch basis. The patches labeled "patch-D1", "patch-D2" and "patch-H" denote the regions that represent inner and outer disk regions (-D1 and -D2) and a halo (-H) region, respectively. These representative regions will be used to show how the results vary in the different regions.

Our observations were conducted on November 23, 2014

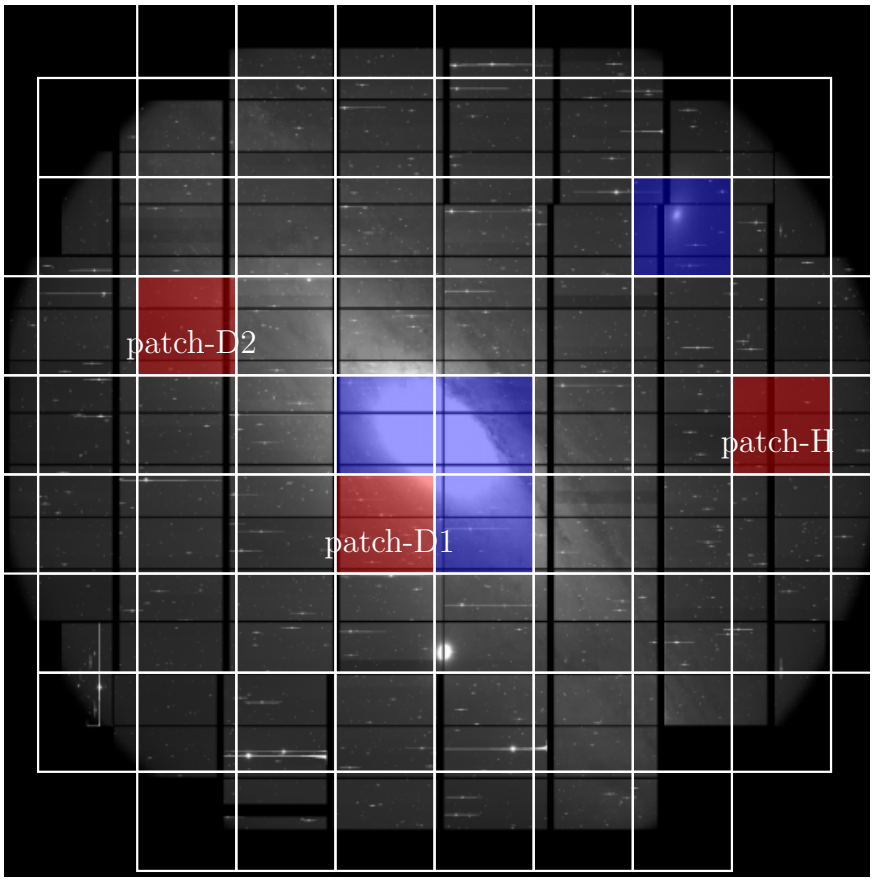

Figure 4. The background image of M31 shows configuration of 104 CCD chips of the Subaru/HSC camera. The white-color grids are the HSC "patch" regions. The patches labeled as "patch-D1", "patch-D2" and "patch-H" are taken from representative regions of the disk region closer to the central bulge, the outer disk region and the halo region, respectively, which are often used to show example results of our data processing in the main text. The dark-blue regions are the patches we exclude from our data analysis due to too dense star fields, where fluxes from stars are saturated and the data are not properly analyzed.

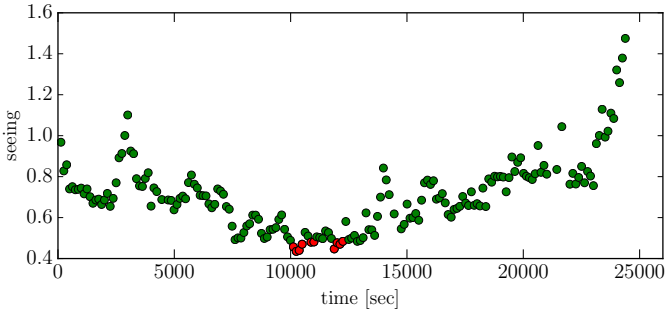

Figure 5. The PSF FWHM (seeing size) of each exposure (90 sec exposure each) as a function of time t [sec] from the start of our observation. We took the images of M31 region every 2 min (90 sec exposure plus about 35 sec for readout), and have 188 exposures in total. The red points show the 10 best-seeing images ($\sim 0.45''$) from which the reference image, used for the image difference, was constructed.

which was a dark night, a day after the new moon. In total, we acquired 194 exposures of M31 with the HSC r-band filter[8], for the period of about 7 hours, until the elevation of M31 fell below about 30 degrees. We carried out the observations with a cadence of 2 minutes, which allows us to densely sample the light curve for each variable object. The total exposure time was 90 seconds on source and about 35 seconds were spent for readout on average. The weather was excellent for most of our observation as can be seen from Fig. 5, which shows how the seeing FWHM changed with time from the start of our observation. The seeing size was better than $0.7''$ for most of the observation period, with a best seeing FWHM of about $0.4''$ at $t \sim 10,000$ sec (2.8 hours). However, the seeing got worse than $1''$ towards the end of our observation. We exclude 6 exposures which had seeing FWHM worse than $1.2''$ and use the remaining 188 exposures for our science analysis.

We also use the g- and r-band data, which were taken during the commissioning run on June 16 and 17 in 2013, respectively, in order to obtain color information of stars as well as to test a variability of candidates at different epochs. The g-band data consist of 5×120 sec exposures and 5×30 sec exposures in total, while the r-band data consists of 10×120 sec exposures.

3.2. *Data reduction and Sample selection*

3.2.1. *Standard data processing*

We performed basic standard data reduction with the dedicated software package for HSC, `hscPipe` (version 3.8.6; also see Bosch et al. in preparation), which is being developed based on the Large Synoptic Survey Telescope software pack-

[8] See http://www.naoj.org/Projects/HSC/forobservers.html for the HSC filter system

age (Ivezic et al. 2008; Axelrod et al. 2010; Jurić et al. 2015) [9]. This pipeline performs a number of common tasks such as bias subtraction, flat fielding with dome flats, coadding, astrometric and photometric calibrations, as well as source detection and measurements.

After these basic data processing steps, we subtract the background contamination from light diffusion of atmosphere and/or unknown scattered light. However the background subtraction is quite challenging for the M31 region, because there is no blank region and every CCD chip is to some extent contaminated by unresolved, diffuse stellar light. To tackle this problem, we first divide each CCD chip into different meshes (the default subdivision is done into 64 meshes in each CCD chip). We then employ a higher-order polynomial fitting to estimate a smooth background over different meshes. We employed a 10-th order polynomial fitting for the CCD chips around the bulge region, which are particularly dense star regions. For other CCD chips, we use a 6-th order polynomial fitting scheme. However, we found residual systematic effects in the background subtraction, so we will further use additional correction for photometry of the difference image, as we will discuss later.

For our study, accurate PSF measurements and accurate astrometric solutions are crucial, because those allow for an accurate subtraction of different images. The pipeline first identifies brightest star objects ($S/N \gtrsim 50$) to characterize the PSF and do an initial astrometric and photometric calibration. From this initial bright object catalog, we select star candidates in the size and magnitude plane for PSF estimation (see Bosch et al. for details). The selected stars are fed into the PSFEx package (Bertin 2011) to determine the PSF as a function of positions in each CCD chip. The functional form of the PSF model is the native pixel basis and we use a second-order polynomial per CCD chip for interpolation. For the determination of the astrometry, we used a 30 sec calibration image that we took at the beginning of our observation, where bright stars are less saturated. We obtain an astrometry solution after every 11 images, 30 sec calibration frame plus 10 time-consecutive science exposures, by matching the catalog of stars to the Pan-STARRS1 system (Schlafly et al. 2012; Tonry et al. 2012; Magnier et al. 2013). The HSC pipeline provides us with a useful feature, the so-called "hscMap", which defines a conversion of the celestial sphere to the flat coordinate system, "hscMap coordinate", based on a tessellation of the sky. In Fig. 4 the white-color regions denote the hscMap "patch" regions. We perform image difference separately on each patch. Due to too many saturated stars in the bulge region and M101, we exclude the patches, marked by dark blue color, from the following analysis.

3.2.2. *Image subtraction and Object detection*

In order to find variable objects, we employ the difference image technique developed in Alard & Lupton (1998) (also see Alard 2000), which is integrated into the HSC pipeline. To do this, we first generated the "reference" image by co-adding 10 best-seeing images among the 188 exposure images, where the 10 images are not time-consecutive (most of the 10 images are from images around about 3 hours from the beginning of the observation, as shown in Fig. 5). We use the mean of the 10 images as the observation time of the reference image, $t_{\rm ref}$, which is needed to model the microlensing light curve (Eq. 18).

In order to make a master catalog of variable object candidates, we constructed 63 target images by co-adding 3 time-consecutive images from the original 188 exposure images. A typical limiting magnitude is about 26 mag (5σ for point sources), and even better for images where seeing is good (see below). When subtracting the reference image from each target image, the Alard & Lupton algorithm uses a space-varying convolution kernel to match the PSFs of two images. The optimal convolution kernel is derived by minimizing the difference between convolved PSFs of two images. A variable object, which has a flux change between the two images, shows up in the difference image.

Fig. 6 shows the result of the image subtraction performed by the pipeline. Even for a dense star region in M31, the pipeline properly subtracts the reference from the target image, by matching the PSFs and astrometry. A point source which undergoes a change in its flux shows up in the difference image, as seen in the right panel. In this case, the candidate appears as a black-color point source meaning a negative flux, because it has a fainter flux in the target image than in the reference image.

We detect objects in the difference image each of which is defined from a local minimum or maximum in the difference image, where we used 5σ for the PSF magnitude as detection threshold. The pipeline also measures the center of each object and the size and ellipticity from the second moments. In this process we discarded objects that have ill-defined center, a saturated pixel(s) in the difference and/or original image or if the objects are placed at a position within 50 pixels from the CCD edge.

3.2.3. *PSF photometry and master catalog of variable star candidates*

For each variable star candidate, we obtain PSF photometry in the difference image to quantify the change of flux. We allow negative PSF fluxes for candidates that have fainter flux in the target image than in the reference image. Since the photon counts in each CCD pixel is generally contaminated by multiple stars in most of the M31 regions, we often find a residual coherent background (large-scale modulated background) in each difference image, due to imperfect background subtraction in the original image. To avoid contamination from such a residual background, we first measure the spatially constant background from the median of counts in 41×41 pixels around each object in the postage-stamp image, and then subtract this background from the image. Then we perform the PSF-photometry counts in ADU units taking the PSF center to be at the candidate center. Hereafter we sometimes refer to PSF magnitude in the difference image as "PSF counts". The pipeline also estimates noise in each pixel assuming the background limit (Poisson noise), and gives an estimation of the noise for the PSF photometry (see equations 14 and 15 for the similar definition in Mandelbaum et al. 2014). However, the noise estimation involves a non-trivial propagation of Poisson noise in the image difference procedures, so we will use another estimate for the PSF photometry error in each patch, as described below.

In the following we focus on the PSF photometry counts in ADU units in the difference image, rather than the magnitude, because it is the direct observable. However, we will also need to infer the magnitude of each candidate; for example, to estimate the luminosity function of source stars in each magnitude bin or to plot the light curve of variable star candi-

[9] Also see http://www.astro.princeton.edu/~rhl/photo-lite.pdf for details of the algorithm used in the pipeline.

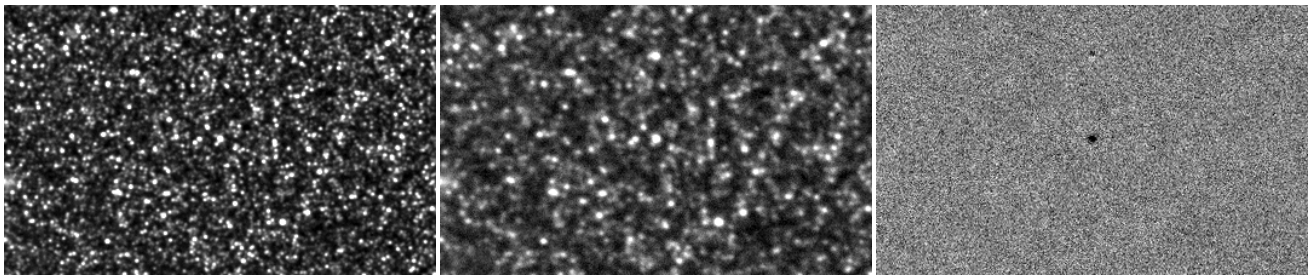

Figure 6. An example of the image subtraction technique we use for the analysis in this paper. The left-panel image is the reference image which was constructed by co-adding the 10 best-seeing data, with typical seeing of 0.45″ (see Fig. 5). The size of the image is 222×356 pixels (corresponding to about 0.63 sq. arcmin), which is taken from "patch-D2" in Fig. 4. The middle panel is the target image (coadded image of 3 exposures) whose seeing size is 0.8″. The right panel shows the difference image, showing that the pipeline properly subtracts the two images even for such a dense star region and a variable star candidate shows up at the center. In this case, the candidate object appears as a negative flux in the difference image, because the object has a fainter flux in the target image than in the reference image.

dates in units of the magnitude. In this case we estimate the magnitude of an object in the i-th target image, m_i, based on

$$m_i = -2.5 \log\left(\frac{C_{\mathrm{diff},i} + C_{\mathrm{ref}}}{F_{0,i}}\right), \tag{20}$$

where C_{diff}, i is the PSF flux for the object in the difference image of the i-th target image, C_{ref} is the PSF flux of the reference image at the object position, and $F_{0,i}$ is the zero-point flux in the i-th image. Note that the counts of the reference image C_{ref} can be contaminated by fluxes from neighboring stars, so the above magnitude might not be accurate.

From the initial catalog constructed from the 5σ candidates from the 63 coadded images, we prune it down to a *master* catalog of "secure" variable star candidates by applying the following criteria:

- *PSF magnitude threshold* – A candidate should have a PSF magnitude, with a detection significance of 5σ or higher (including a negative flux), in any of the 63 difference images.
- *Minimum size* – The size of the candidate should be greater than 0.75 times the PSF size of each difference image.
- *Maximum size* – The size of the candidate should be smaller than 1.25 times the PSF size.
- *Roundness* – The candidate should have a round shape. We require our candidates to have an axis ratio greater than 0.75, as the PSF does not show extreme axis ratios.
- *PSF shape* – We impose that the shape of an object should be consistent with the PSF shape. The residual image, obtained by subtracting a scaled PSF model from the candidate image in the difference image, should be within 3σ for the cumulative deviation over pixels inside the PSF aperture.

Fig. 7 shows examples of objects that pass or fail the above criteria. Note that the above conditions are broad enough in order for us not to miss a real candidate of microlensing if it exists. We make a master catalog of variable star candidates from objects that pass all the above conditions as well as are detected in the image difference at least twice in the 63 difference images at the same position within 2 pixels. These criteria result in 15,571 candidates of variable objects, which is our master catalog of variable star candidates.

3.2.4. *Light curve measurement*

Once each candidate is identified, we measure the PSF counts in each of the 63 difference images. This allows us to measure the light curve with a 6 min resolution, as a function of time from the beginning to the end of our 7 hour long observations. In order to restore the highest time resolution of our data, we then used each of 188 exposures and measured the PSF counts in each of the 188 difference image that was made by subtracting the reference image (the coadded image of 10 best-seeing exposures) from every single exposure. Here we used the same position of candidate as used in the 63 images. In this way we measure the light curve of the object with 2 min time resolution.

Fig. 8 shows the light curves for examples of real variable stars. Note that we converted the PSF counts of each candidate in the difference image to the magnitude based on Eq. (20). However, the magnitude might be contaminated by fluxes from blended stars surrounding the candidate star. This demonstrates our ability to properly sample the light curves with high time resolution. Thus the figure shows that the difference image technique works well and can identify variable star candidates as well as measure their light curves.

Fig. 9 shows the distribution of secure variable star candidates detected in our analysis over the HSC field-of-view, for candidates with magnitudes $m_r \leq 24$ and 25 mag in the left and right panel, respectively. To estimate the magnitude of each candidate, we used the PSF magnitude of the candidate in the reference image. Based on the shape of the light curve for each candidate, we visually classified the candidates in different types of variable stars; i) stellar flares, ii) eclipsing or contact binary systems, iii) asteroids (moving object), iv) Cepheid variables if the candidates appear to have a longer period than our observation duration (7 hours), and v) "fakes". Here fakes are those candidates which show time variability only when the seeing conditions are as good as $\lesssim 0.6''$. Since such good-seeing data is deeper as found from Figs. 5 and 10, we seem to find RR-Lyrae type variables whose apparent magnitudes would be around $r \sim 25$ mag. When the seeing gets worse, these stars cannot be reliably seen in the difference image. Since RR-Lyrae stars should exist in the M31 region, we think the "fake" stars are good candidates for RR-Lyrae stars. The figure shows that our analysis successfully enables to find variable stars across the disk and halo regions. The total number of candidates are 1,334 and 2,740 for $m_r \leq 24$ and 25 mag, respectively.

4. STATISTICS AND SELECTION CRITERIA

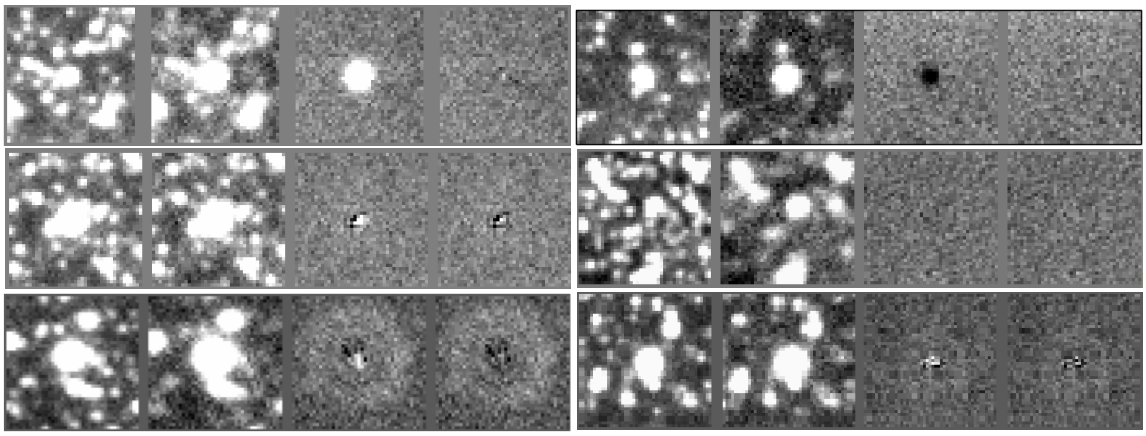

Figure 7. Examples of detected objects in the difference image, which pass or do not pass the selection criteria to define a master catalog of variable star candidates (see text for details). Each panel shows 4 postage-stamp images: the leftmost image is the reference image (the coadded image of 10 best-seeing exposures), the 2nd left is the target image (the coadded image of 3 time-consecutive exposures), the 3rd image is the difference image between the reference and target images, and the rightmost image is the residual image after subtracting the best-fit PSF image from the difference image at the object position. The two objects in top raw are successful candidates that passed all the selection criteria: the left-panel object has a brighter flux in the target image than in the reference image, while the right-panel object has a fainter flux (therefore appear as a black-color image with negative flux). The lower-row objects are removed from the catalog after the selection criteria. The objects in the middle row are excluded because the object is either smaller or larger than the PSF size. The left object in the bottom row is excluded because it has a too large ellipticity than PSF. The right object is excluded because of too large residual image.

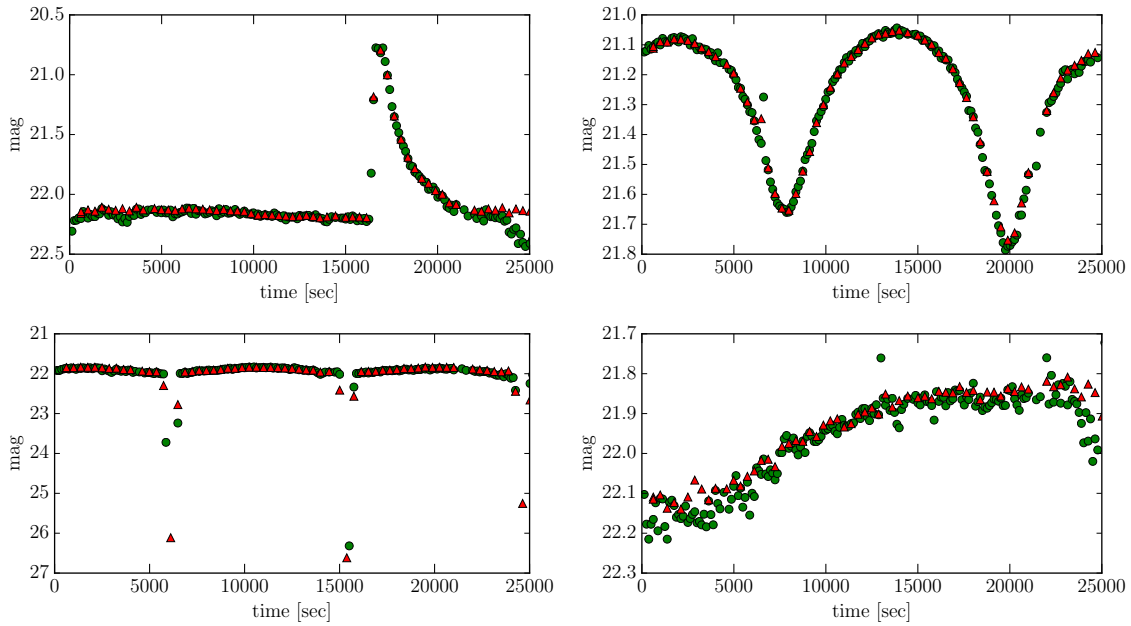

Figure 8. Examples of light curves for real variable stars identified in our method. The green-circle data points show the light curve sampled by our original data of 2 min sampling rate, while the red-triangle points are the light curve measured from the coadded data of 3 time-consecutive exposures (therefore 6 min cadence) (see text for details). *Upper left*: candidate stellar flare. When converting the magnitude from the counts in the difference image at each observation time, we used Eq. (20). Note that the estimated magnitude might be contaminated by fluxes of neighboring stars in the reference image. *Upper right*: candidate contact binary stars. *Lower left*: the eclipse binary system, which is probably a system of white dwarf and brown dwarf, because one star (white dwarf) has a total eclipse over about 10 min duration, and then the eclipse has about 3hours period. *Lower right*: candidate variable star, which has a longer period than our observation duration (7 hours).

Given the catalog of variable star candidates each of which has its measured light curve, we now search for secure candidates of PBH microlensing. In this section we describe our selection criteria to discriminate the microlensing event from other variables.

4.1. *Photometric errors of the light curve measurement*

Our primary tool to search for variable objects in the dense star regions of M31 is the use of the image difference technique, as we have shown. To robustly search for secure candidates of PBH microlensing that have the expected light curve shapes, it is crucial to properly estimate the photometry error in the light curve measurement. However, accurate photometry for dense star regions in M31 is challenging. To overcome this difficulty, we use the following approach to obtain a conservative estimate of the error. The pipeline performs image subtraction on each patch basis (as denoted by white-color square regions in Fig. 4). For a given difference image, we randomly select 1,000 points in each patch region, and then perform PSF photometry at each random point in the same manner as that for the variable star candidates. In selecting random points, we avoided regions corresponding to bad CCD

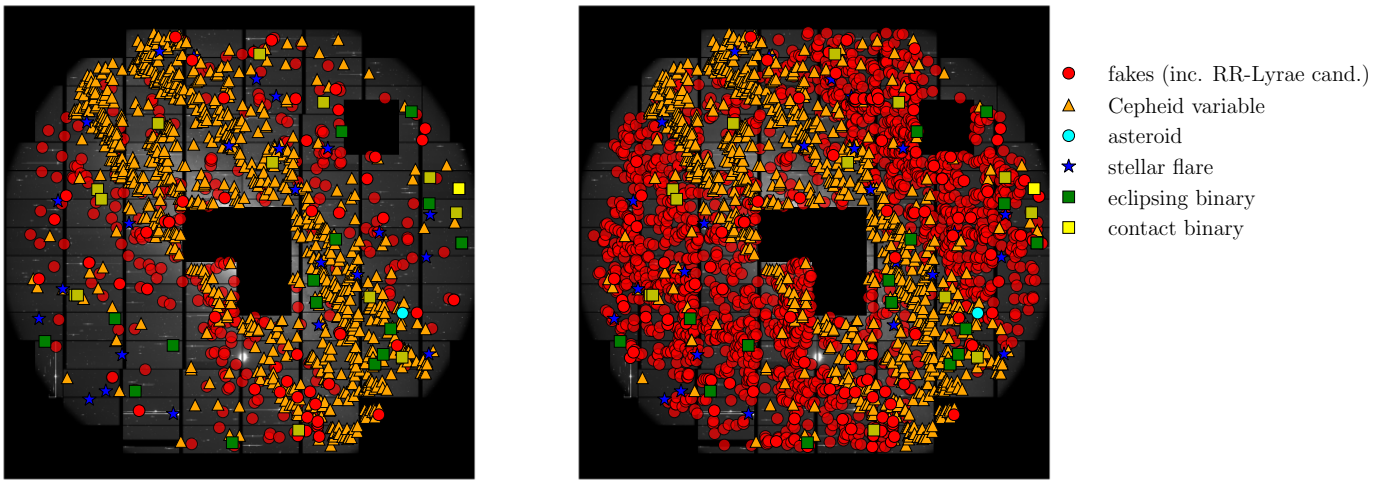

Figure 9. Distribution of secure variable star candidates, detected from our analysis using the image difference technique. The different symbols denote different types of candidates classified based on the shapes of their light curves. Here we exclude other non-secure candidates that are CCD artifacts and fake events near to the CCD edge or bright stars. The left panel shows the distribution for the candidates with magnitudes $m_r \leq 24$ mag, while the right panel shows the candidates at $m_r \leq 25$ mag. The number of candidates are 1,334 and 2,740, respectively.

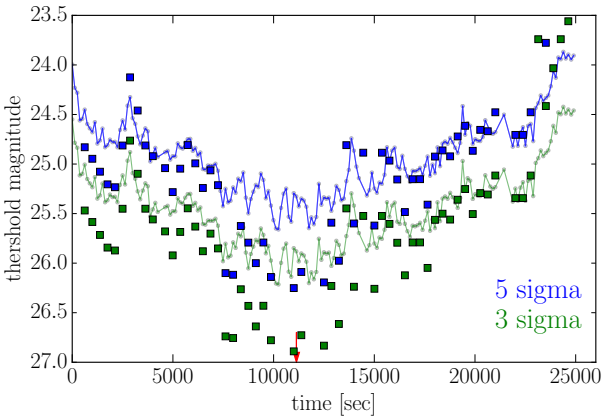

Figure 10. The photometric error used for the light curve measurement in the difference image; we randomly select 1,000 points in the difference image of a given patch (here shown for the patch-D2 in Fig. 4), measure the PSF photometry at each random point, and then estimate the variance of the PSF photometries (see text for details). The square symbols show the 3- or 5-sigma photometric errors estimated from the variance when using the difference images constructed from the coadded images of 3 exposures, as a function of observation time. The circle symbols, connected by the line, are the results for each exposure. Although we use the photometric error in the ADU counts for a fitting of the microlensing model to the light curve, we here convert the counts to the magnitude for illustrative convenience.

pixels or near the CCD chip edges. We then estimate the variance from those 1,000 PSF magnitudes, repeat the variance estimation in the difference image for every observation time, and use the variance as a 1σ photometry error in the light curve measurement at the observation time. The photometric error estimated in this way would include a contamination from various effects such as a large-scale residual background due to an imperfect background subtraction. We find that the photometric error is larger than the error estimated from the pipeline at the candidate position, which is locally estimated by propagating the Poisson noise of the counts through the image subtraction processes.

Fig. 10 shows the photometric error on the light curve measurement in the difference image, estimated based on the above method. The shape of the photometric error appears to correlate with the seeing conditions in Fig. 5. The figure shows that most of our data reaches a depth of 26 mag or so thanks to the 8.2m large aperture of Subaru.

4.2. *Microlensing model fit to the light curve data*

Here we describe our selection procedure for PBH microlensing events from the candidates. The unique part of our study is the the high cadence for the light curve of each candidate, sampled by every 2 min over about 7 hours. However the monitoring of each light curve is limited by a duration of 7 hours. If a microlensing event has a longer time duration than 7 hours, we can not identify such a candidate. We use the statistics in Table 1 to quantify the characteristics of each light curve. Our selection procedure for the candidates are summarized in Table 2. We will describe each of the selection steps in detail.

As we described, we start with the master catalog of variable star candidates, which contains 15,571 candidates, to search for microlensing events. Our level 1 requirement is that a candidate event should have a "bump" in its light curve, defined as 3 time-consecutive flux changes each of which has a signal-to-noise ratio greater than 5σ in the difference image; $\Delta C_i \geq 5\sigma_i$, where the subscript i denotes the i-th difference image (at the observation time t_i). This criteria leaves us with 11,703 candidates over all the patches.

Next we fit the observed light curves of each candidate with a model describing the expected microlensing light curve. As we described in Section 2.3, the light curve of a microlensing in the difference image is given as

$$\Delta C(t_i) = C_0 \left[A(t_i) - A(t_{\rm ref})\right], \tag{21}$$

where C_0 is the PSF-photometry counts of an unlensed image in the difference image, corresponding to F_0 in Eq. (18), and $A(t_i)$ and $A(t_{\rm ref})$ are lensing magnifications at the observation time t_i and the time of the reference image $t_{\rm ref}$. As described in Section 2.3, the light curve in the difference image is char-

Table 1
Definitions of Statistics

Statistic	Definition
$\Delta C(t_i)$	PSF-photometry counts of a candidate in the i-th difference image at the observation time t_i; the time sequence of $\Delta C(t_i)$ forms the light curve of each candidate (188 data points, sampled by every 2 min).
$\Delta C_{\rm coadd}(t_i)$	PSF-photometry counts of a candidate in the i-th difference image of 3 coadded images at t_i (63 data points, sampled by every 6 min)
σ_i	1σ error of PSF-photometry in the i-th difference image (see text for details)
$\sigma_{{\rm coadd},i}$	1σ error in the i-th difference image of 3 coadded images at t_i
bump	sequence of 3 or more time-consecutive data points with $\Delta C_i \geq 5\sigma_i$ in the light curve
bumplen	length (number) of time-consecutive data points with $\Delta C_i \geq 5\sigma_i$
mlchi2_dof	χ^2 of the light curve fit to microlensing model divided by the degrees of freedom
mlchi2in_dof	χ^2 of the microlensing fit for data points with t_i satisfying $t_0 - t^{\rm obs}_{\rm FWHM} \leq t_i \leq t_0 + t^{\rm obs}_{\rm FWHM}$
asymmetry $a_{\rm asy}$	$(1/N_{\rm asy})\ \sum_{t_i}\ [\Delta C(t_0 - \Delta t_i) - \Delta C(t_0 + \Delta t_i)] \Big/ [\overline{\Delta C} - \Delta C_{\rm min}]$ (see text for details)
seeing_corr	correlation between the light curve shape and the seeing variation (see text for details)

Table 2
Selection Criteria

Selection Criterion	Purpose	No. of remained candidates
$\Delta C_{{\rm coadd},i} \geq 5\sigma_{{\rm coadd},i}$	initial definition of candidates	15,571
bumplen≥ 3	select candidates with a significant peak(s) in the light curve	11,703
mlchi2dof< 3.5	select candidates whose light curve is reasonably well fit by the microlensing	227
$a_{\rm asy} < 0.17$	remove candidates that have an asymmetric light curve such as star flares	146
significant peak	select candidates that show a clear peak in its light curve (see text for details)	66
visual inspection	visually check whether the light curve looks a microlensing event	1
seeing_corr	remove candidates whose light curve is correlated with time variation of seeing	1

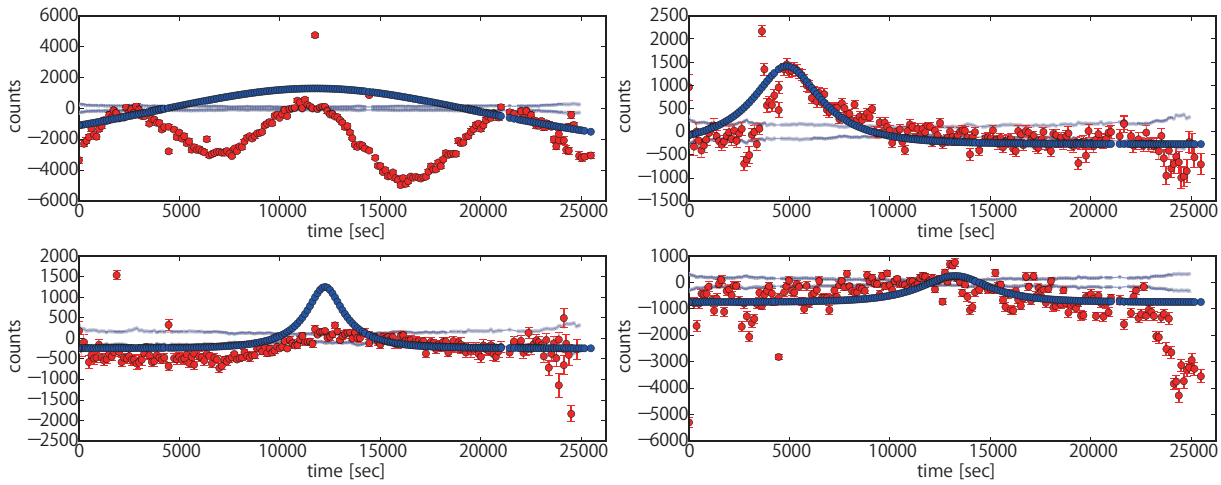

Figure 11. Example of the light curves of candidates that are rejected by our selection criteria for a microlensing event. The red points in each panel shows the PSF photometry at each observation time and consist of 188 data points to form the light curve sampled by every 2 min in the difference images. The errorbar around each data point is the photometry error that is locally estimated by propagating the Poisson noise of counts through the difference image processes at the candidate position. The range bracketed by the two data points around zero counts is the $\pm 1\sigma$ photometry error that is estimated from the PSF photometries of 1,000 random points as shown Fig. 10. The blue data points are the light curve for the best-fit microlensing model. The upper-left panel shows an example of the candidates that is rejected due to a bad $\chi^2_{\rm min}$ for the fitting to the microlensing light curve. The upper-right panel shows an example of the candidates that is rejected by the asymmetric shape of the light curve around the peak. The lower two panels show examples of the candidates that do not show a prominent peak feature as expected for a microlensing event.

acterized by 3 parameters: $(u_{\rm min}, t_{\rm FWHM}, C_0)$, where $u_{\rm min}$ is the impact parameter of closest approach between PBH and a source star in units of the Einstein radius, and $t_{\rm FWHM}$ is the FWHM timescale of the light curve.

We identify the time of maximum magnification in the light curve and denote it by t_0. For the model fitting, we employ the following range for the model parameters:

- $0.01 \leq u_{\rm min} < 1$, which determines the maximum magnification, $A_{\rm max} \equiv A(u_{\rm min})$ (see Eq. 1). Thus we assume the range of maximum magnification to be $1.34 \leq A_{\rm max} \lesssim 100$.
- $0.01 \leq t_{\rm FWHM}/[{\rm sec}] < 25,000$. Here the lower limit is much shorter than the sampling rate of light curve (2 min), but we include such a short time-scale light curve for safety (see below). The upper limit corresponds to the longest duration of our observation ($\sim$ 7 hours).
- Once the parameters, $u_{\rm min}$ and $t_{\rm FWHM}$, are specified, the intrinsic flux can be estimated as $C_0 = \Delta C^{\rm obs}_{\rm max}/[A_{\rm max} -$

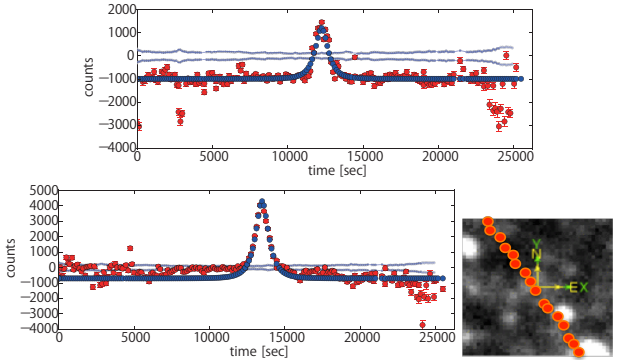

Figure 12. The upper panel shows an example of light curves for fake events that are caused by a spike-like image around a bright star. The light curve appears to look like a microlensing event, but it is found to be near a bright star. The lower panel shows the light curve for an asteroid that also shows a microlensing-like light curve. If the PSF photometry is made at the fixed position (the center in the lower-right image), the measured light curve looks like a microlensing event. The red points in the image denotes the asteroid trajectory. From our analysis of M31 observation, we identified one asteroid.

$A(t_{\rm ref})$], where $\Delta C^{\rm obs}_{\rm max}$ is the counts of the light curve peak in the difference image. In practice, the flux measurement is affected by measurement noise as well as the sampling resolution of light curve, so we allow the intrinsic flux to vary in the range of $0.5\times\Delta C^{\rm obs}_{\rm max}/(A_{\rm max}-1) \leq C_0 \leq 1.5\times\Delta C^{\rm obs}_{\rm max}/(A_{\rm max}-1)$.

The above ranges of parameters are broad enough in order for us not to miss a real candidate of microlensing. For each candidate, we perform a standard χ^2 fit by comparing the model microlensing light curve to the observed light curve:

$$\chi^2 = \sum_{i=1}^{188} \frac{\left[\Delta C^{\rm obs}(t_i) - \Delta C^{\rm model}(t_i; C_0, t_{\rm FWHM}, u_{\rm min})\right]^2}{\sigma_i^2}, \quad (22)$$

where $\Delta C^{\rm model}(t_i)$ is the model light curve for microlensing, given by Eq. (21), and σ_i is the rms noise of PSF photometry in the i-th difference image, estimated from the 1,000 random points as described above.

We compute the reduced χ^2 by dividing the minimum χ^2 by the degrees of freedom (188-3=185). We discard candidates that have mlchi2_dof > 3.5. This criterion is reasonably conservative (the P-value is $\sim 10^{-5}$). We further impose the condition that the best-fit $t_{\rm FWHM} < 14,400$ sec (4 hours), in order to remove candidates whose light curve has a longer time variation than what we can robustly determine. This selection removes most of Cepheid-type variables. This selection leaves 225 candidates. The upper-left panel of Fig. 11 shows an example of candidates that are removed by the condition mlchi2_dof < 3.5 (i.e. mlchi2_dof > 3.5 for this candidate). This is likely to be a binary star system.

Microlensing predicts a symmetric light curve with respect to the maximum-magnification time t_0 ($A_{\rm max}$); the light curve at $t_i = |t_0 \pm \Delta t|$ should have a similar flux as the lensing PBH should have a nearly constant velocity within the Einstein radius. Following Griest et al. (2014), we define a metric to quantify the asymmetric shape of the light curve,

$$a_{\rm asy} = \frac{1}{N_{\rm asy}} \sum_{t_i \in |t_0 \pm t^{\rm obs}_{\rm FWHM}|} \frac{|\Delta C(t_0 - \Delta t_i) - \Delta C(t_0 + \Delta t_i)|}{\overline{\Delta C} - \Delta C_{\rm min}}. \quad (23)$$

Here $t^{\rm obs}_{\rm FWHM}$ is the timescale that the observed light curve declines to half of its maximum value. For this purpose, we take the longer of the timescales from either side of the two half-flux points from the maximum peak. If the expected half-flux data point is outside the observation window of light curve, we take the other side of the light curve to estimate $t^{\rm obs}_{\rm FWHM}$. The summation runs over the data points satisfying $t_i \leq |t_0 \pm t^{\rm obs}_{\rm FWHM}|$, 2 times the FWHM timescale around the light curve peak. Note that, if the summation range is outside the observation window, we take the range $|t_0 \pm (t_0 - t_{\rm start})|$ or $|t_0 \pm (t_{\rm end} - t_0)|$, where $t_{\rm start}$ or $t_{\rm end}$ is the start or end time of the light curve. $N_{\rm asy}$ is the number of data points in the above summation, $\overline{\Delta C}$ is the average of the data points taken in the summation, and $\Delta C_{\rm min}$ is the minimum value of the counts.

By imposing the condition $a_{\rm asy} < 0.17$, we eliminate candidates that have an asymmetric light curve, and we have confirmed that this condition eliminates most of the star flare events from the data base. This condition also eliminates some of the variable stars that are likely to be Cepheids. After this cut the number of candidates is reduced to 146. The upper-right panel of Fig. 11 shows an example of the candidates that are removed by the condition $a_{\rm asy} < 0.17$.

In addition we discard candidates, if the observed light curve does not have any significant peak; e.g., we discard candidates if mlchi2in_dof > 3.5 (see Table 1 for the definition) or if the time of the light-curve peak is not well determined. The lower panels of Fig. 11 show two examples of such rejected candidates, which do not show a clear bump feature in the light curve as expected for microlensing. This selection cut still leaves us with 66 candidates.

Finally we perform a visual inspection of each of the remaining candidates. We found various fake events that are not removed by the above automated criteria. Most of the fake events are caused by an imperfect image subtraction; in most cases the difference image has significant residuals near the edges of CCD chips and around bright stars. In particular, bright stars cause a spiky residual image in the difference image, that results in fake candidates that have microlensing-like light curve if measured at a fixed position. We found 44 fake events caused by such spike-like images around bright stars. There are 20 fake events around the CCD edges. The upper panel of Fig. 12 shows an example of spike-like fakes. We were also able to identify 1 fake event caused by a moving object, an asteroid. If the light curve is measured at the fixed position which the asteroid is passing, it results in a light curve which mimics microlensing, as shown in the lower panel of Fig. 12.

Thus our visual inspection leads us to conclude that 65 events among 66 remaining candidates are fake and we end up with one candidate event which passes all our cuts and visual checks. The candidate position is (RA, dec) = (00h 45m 33.413s, +41d 07m 53.03s).

Fig. 13 shows the images and the light curve for this candidate of microlensing event. Although the light curve looks noisy, it is consistent with the microlensing prediction. The magnitude inferred from the reference image implies that the candidate has a magnitude of $r \sim 24.5$ mag. The obvious question to consider is whether this candidate is real. Unfortunately, the candidate is placed outside the survey regions of the Panchromatic Hubble Andromeda Treasury (PHAT) catalog in Williams et al. (2014) (also see Dalcanton et al. 2012) [10], so the HST image is not available. It is unclear if there are

[10] https://archive.stsci.edu/prepds/phat/

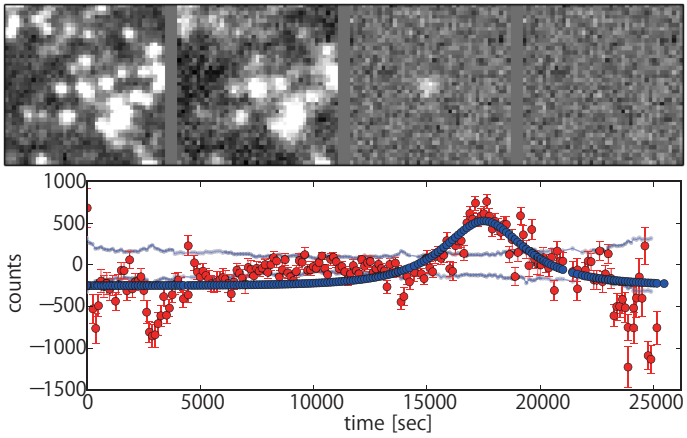

Figure 13. One remaining candidate that passed all the selection criteria of microlensing event. The images in the upper plot show the postage-stamped images around the candidate as in Fig. 7: the reference image, the target image, the difference image and the residual image after subtracting the best-fit PSF image, respectively. The lower panel shows that the best-fit microlensing model gives a fairly good fitting to the measured light curve.

any variable stars that could produce the observed light curve, with a single bump. To test the hypothesis that the candidate is a variable star, we looked into the *r*-band data that was taken in the commissioning run in 2013, totally different epoch from our observing night. However, the seeing condition of the *r*-band is not good (about 1.2″), so it is difficult to conclude whether the star pops out of the noise in the difference images. Similarly we looked into the *g*-band images taken in the HSC commissioning run. However, due to the short duration of the data itself (∼ 15 min), it is difficult to judge whether this candidate has a time variability between the *g* images. Hence we cannot draw any convincing conclusion on the nature of this candidate. In what follows, we derive an upper bound on the abundance of PBHs as a constituent of DM for both cases where we include or exclude this remaining candidate.

5. RESULTS: UPPER BOUND ON THE ABUNDANCE OF PBH CONTRIBUTION TO DARK MATTER

In this section we describe how we use the results of our PBH microlensing search to derive an upper limit on the abundance of PBHs assuming PBHs consist of some fraction of DM in the MW and M31 halos. In order to do this, we need three ingredients – (1) the event rates of microlensing as we estimated in Section 2.2, (2) a detection efficiency for PBH microlensing events, which quantifies the likelihood of whether a microlensing event, even if it occurs during our observation duration, will pass all our selection cuts, and (3) the number of source stars in M31. In this section we describe how to estimate the latter two ingredients and then derive the upper bound result.

5.1. *Efficiency Calculation: Monte Carlo simulation*

The detection efficiency of PBH microlensing events depends upon the unlensed flux of the star in M31, F_0, and quantifies the fraction of microlensing events with a given impact parameter ($u_{\rm min}$) and time scale ($t_{\rm FWHM}$) that can be detected given our selection cuts.

To estimate the efficiency we carry out simulations of microlensing light curves. We vary the model parameters to generate a large number of realizations of the simulated microlensing light curves. First we randomly select the time of maximum magnification ($t_{\rm max}$) from the observation window, the impact parameter $u_{\rm min} \in [0, 1]$ and the FWHM timescale $t_{\rm FWHM}$ in the range of $0.01 \leq t_{\rm FWHM}/[\rm sec] \leq 25,000$ to simulate the input light curve in the difference image for a given intrinsic flux of a source star, F_0 (more precisely, the intrinsic counts C_0 in the difference image). Then, we add random Gaussian noise to the light curve at each of the observation epochs t_i, estimated from the i-th difference image in a given patch (Section 4.1). For each intrinsic flux, we generate 10,000 simulated light curves in each patch region.

For each simulated light curve, we applied all of our selection cuts (see Section 4 and Tables 1 and 2) to assess whether the simulated event passes all the criteria. Fig. 14 shows the estimated efficiency for a given intrinsic flux of a star as a function of the timescale ($t_{\rm FWHM}$) of the simulated light curve, in the patch-D2 of Fig. 4. A microlensing event for a bright star is easier to detect, if it occurs, because even a slight magnification is enough to identify it in the difference image. On the other hand, a fainter star needs more significant magnification to be detected. If the microlensing timescale is in the range of 4 min $\lesssim t_{\rm FWHM} \lesssim$ 3 hours, the event can be detected by our observation (2 min sampling rate and 7 hours observation). We interpolated the results for different intrinsic fluxes to estimate the detection efficiency for an arbitrary intrinsic flux. We repeated the simulations using the photometry errors to estimate the efficiency for each patch.

We also performed an independent estimation of the detection efficiency. We used fake image simulations where we injected fake microlensing star events into individual HSC images using the software GalSim in Rowe et al. (2015) (also see Huang et al. in preparation), and then re-ran the whole data reduction procedure including image subtraction to measure the light curve. We then assessed whether the fake microlensing event can be detected by our selection criteria. Fig. 15 compares the detection efficiency estimated using the fake image simulations with the results of the simulated light curves (Fig. 14) in the patch-D2. The figure clearly shows that the two results fairly well agree with each other. The fake image simulations are computationally expensive. With the results in Fig. 15, we conclude that our estimation of the detection efficiency using the simulated light curves are fairly accurate.

5.2. *Estimation of star counts in M31*

The expected number of microlensing events depends on the number of source stars in M31. However, since individual stars are not resolved in the M31 field, it is not straightforward to estimate the number of source stars from the HSC data. This is the largest uncertainty in our results, so we will discuss how the results change for different estimations of the source star counts. As a conservative estimate for the number of source stars, we use the number of "detected peaks" in the reference image of M31 data, which has the best image quality (coadding the 10 best-seeing exposures) and is used for the image subtraction. Fig. 16 shows the distribution of peaks identified from the reference image in an example region (with a size 226 × 178 pixels corresponding to about 38″×30″), taken from the patch-D2 region. The figure clearly shows that only relatively bright stars, or prominent peaks, are identified, but a number of faint stars or even bright stars in a crowded (or blended) region will be missed. Thus this estimate of the source star counts is extremely conservative. Nevertheless this is one of the most secure way to obtain source counts, so we will use these counts in each patch region.

The color scale in Fig. 17 shows the total number of peaks in each patch region. It can be seen that a relatively larger

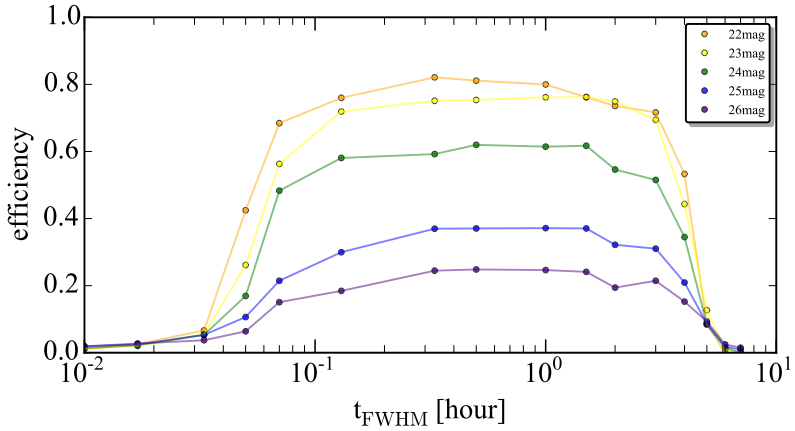

Figure 14. The detection efficiency estimated from light curve simulations taking into account the PSF photometry error in each of 188 target images we used for the analysis (see text for details). Here we generated Monte Carlo simulations of microlensing events randomly varying the three parameters: the impact parameter (or maximum lensing magnification), the FWHM timescale of microlensing light curve (x-axis), and the observation time of the microlensing magnification peak, for source stars of a fixed magnitude as indicated by legend. The detection efficiency for each source magnitude is estimated from 1,000 realizations.

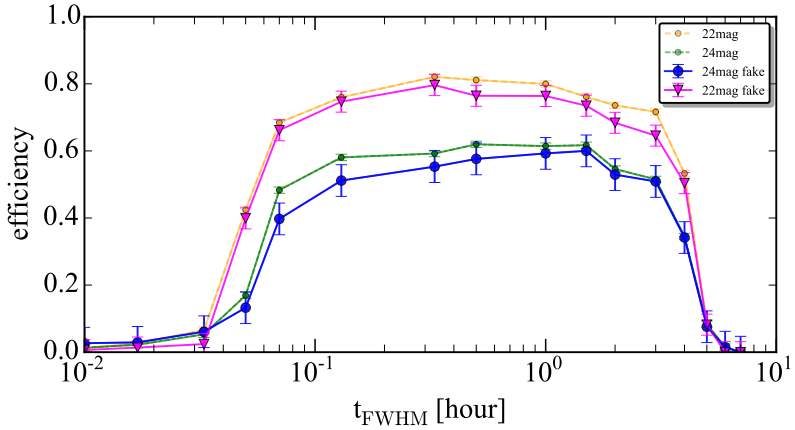

Figure 15. A justification of the detection efficiency estimation, based on the different method using the fake image simulations. We injected fake microlensing star images in individual exposures of the real HSC data (patch-D2 in Fig. 4), re-ran the whole data processing, and assessed whether the fake images pass all the selection criteria for a microlensing event. The small circles show the results from light curve simulations (the same as shown in Fig. 14), and the large symbols show the results from the fake image simulations, for the intrinsic magnitudes of 22 and 24 mag, respectively.

number of the peaks are identified in the outer halo region of M31, because each star can be resolved without confusion. On the other hand, there are less number of resolved peaks in the patches corresponding to the disk region due to crowding. The total number of peaks identified over all the patch regions is about 6.4 million. Fig. 18 shows the surface density of peaks identified in HSC in the disk and halo regions of M31 for the three patches marked in Fig. 4. To estimate the magnitudes for the surface density, we performed PSF photometry of each peak using its location as the PSF center. The figure confirms that more number of peaks are identified in the halo region.

As another justification for the estimation of the source star counts, we compare the number counts of peaks in the HSC image with the luminosity function of stars in the HST PHAT catalog in Williams et al. (2014) (also see Dalcanton et al. 2012), where individual stars are more resolved thanks to the high angular resolution of the ACS/HST data. Since the PHAT HST data was taken with F475W and F814W filters, we need to make color transformation of the HST photometry to infer the HSC r-band magnitude. For this purpose, we first select 100 relatively bright stars in the PHAT catalog. Then we match the HST stars with the HSC peaks by their RA and dec positions, and compare the magnitudes in the HST and HSC photometries. In order to derive the color transformation, we estimated a quadratic relation between the HST and HSC magnitudes for the matched stars in a two-dimensional space of $(m_r^{\rm HSC} - m_{\rm F475W})$ and $(m_{\rm F475W} - m_{\rm F814W})$:

$$m_r^{\rm HSC} = m_{\rm F475W} - 0.0815 - 0.385\,(m_{\rm F475W} - m_{\rm F814W}) \\ -0.024\,(m_{\rm F475W} - m_{\rm F814W})^2\,. \quad (24)$$

We then applied this color transformation to all the PHAT stars. Although the above one-to-one color transformation is not perfect for different types of stars, we do not think that the uncertainty largely affects our main results as we will discuss below.

Fig. 19 compares the surface density of stars in the HST PHAT catalog with that of the HSC peaks, as a function of magnitudes, in the overlapping regions between our M31 data and HST PHAT. These regions correspond to "bricks07" and "bricks11". The figure clearly shows that the HSC peak counts fairly well reproduces the HST results down to $r \sim$

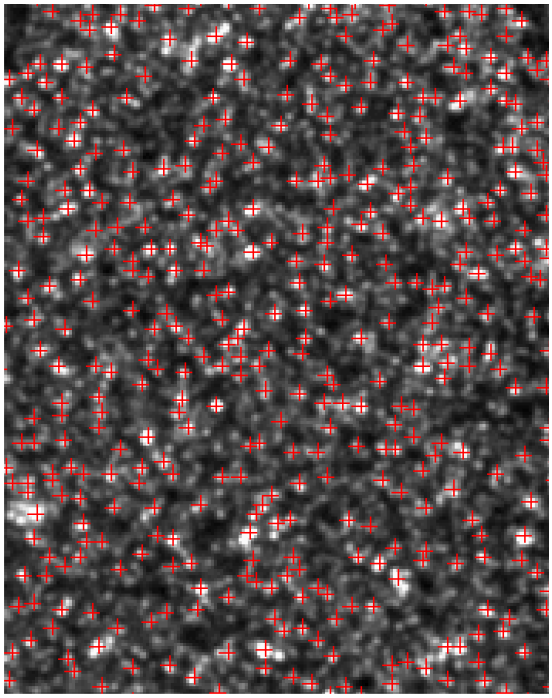

Figure 16. An example image of the distribution of peaks (cross symbols) identified in a small region of the reference image (the coadded image of 10 best-seeing exposures), which has a size of about $38'' \times 30''$ area and is taken from the patch-D2 region. We measure the PSF photometry of each peak, and then use the number of peaks as an estimation of the number of source stars in each magnitude bin.

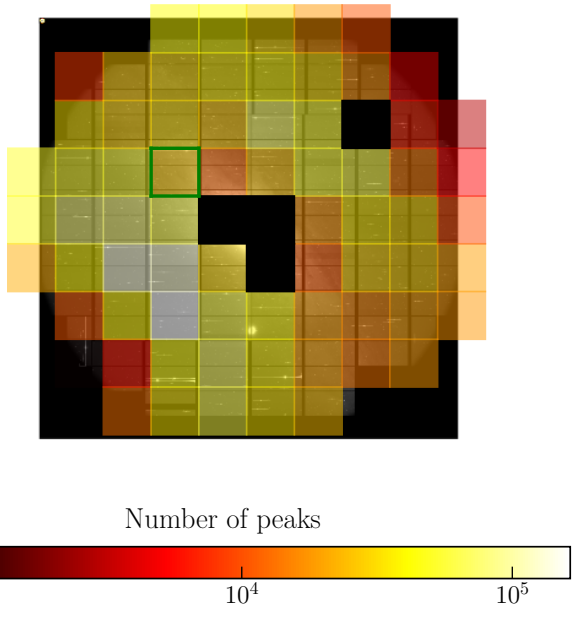

Figure 17. The color scale denotes the total number of detected peaks in each patch region for the HSC data. Note that the black-color patches are excluded from our analysis due to too crowded regions. The number of the peaks in a disk region tends to be smaller than that in a outer, halo region, because stars in a disk region are more crowded and only relatively brighter stars or more prominent peaks are identified.

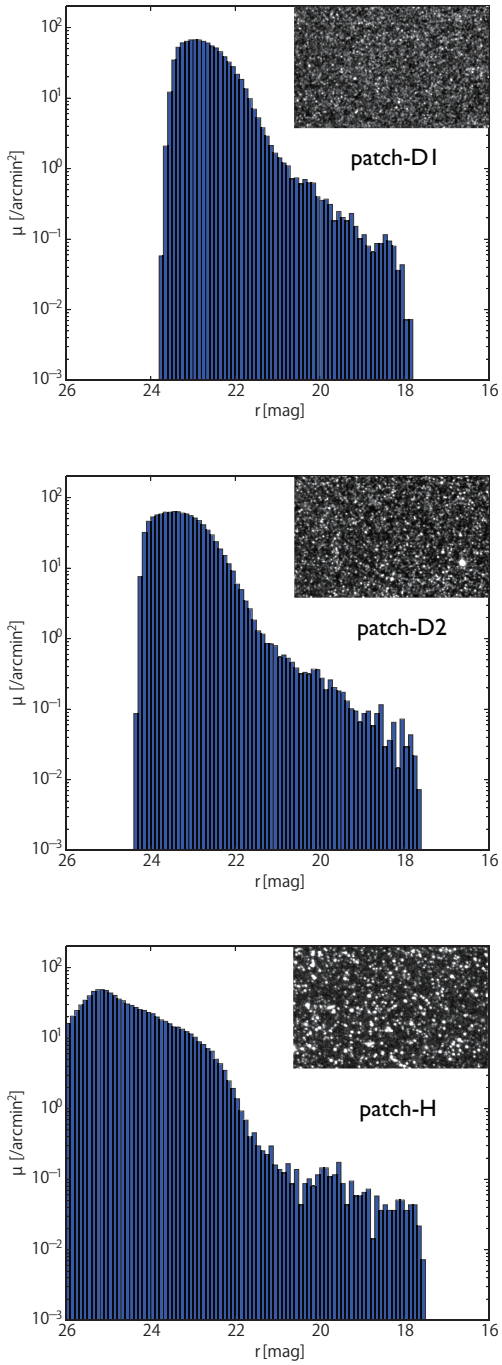

Figure 18. The peaks counts of HSC data in different regions of M31; two disk regions denoted as patch-D1 and patch-D2 and the halo region denoted as patch-H in Fig. 4. The HSC data can find a more number of fainter peaks in the halo regions because individual stars are more resolved and less crowded.

23 mag. Since the HSC photometry of each peak should be contaminated by fluxes of neighboring stars, we would expect a systematic error in the PSF photometry, which causes a horizontal shift in the surface density of peaks (the HSC photometry is expected to over-estimate the magnitude). Even with this contamination, the agreement looks promising. However, it is clear that the HSC peak counts clearly misses the fainter stars, which can be potential source stars for PBH microlens-

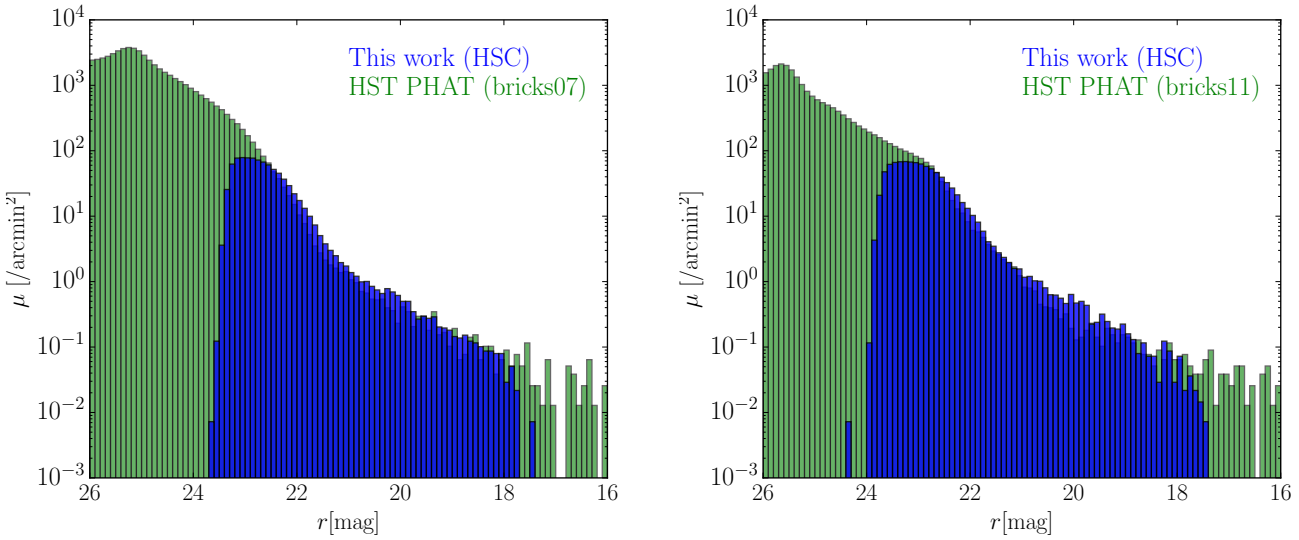

Figure 19. The green histogram shows the luminosity function of M31 stars in the HST PHAT catalog, while the blue histogram shows that of the peaks in the HSC image. We converted the magnitudes of HST stars to the HSC r-band magnitudes using Eq. (24). The comparison is done using the PHAT catalog in the two regions of "bricks07" (or B7) and "bricks11" (B11) in Fig. 1 of Dalcanton et al. (2012), which are contained in the patch right next to or one-upper to the patch-D2 in the HSC data (see Fig. 4). These regions are in a disk region of M31. The luminosity function of HSC peaks fairly well reproduces the HST result down to $r \sim 23$ mag, but clearly misses fainter stars. The PHAT luminosity functions in the two regions appear to be in a similar shape.

ing. The surface density of HST stars in different regions look similar.

The data overlap between HSC and PHAT covers the disk region only partially. Nevertheless, as an optimistic estimate of our star counts, we infer the underlying luminosity function of stars in the disk region from the HST PHAT catalog based on the number counts of HSC peaks at $m_r = 23$ mag in each patch of the disk regions, assuming that the luminosity function of HST stars is universal in the disk regions. For the halo regions, we use the HSC peak counts. In this optimistic estimate of source stars, we find about 8.7×10^7 stars down to $m_r = 26$ mag over the entire region of M31, which is a factor of 14 more number of stars than that of HSC peaks. However, the source stars extrapolated from the HST data are faint, and will suffer from lower detection efficiency. Therefore, the final constraints do not improve a lot from these improved star counts.

One might worry about a possible contamination of dust extinction to the number counts of source stars. However our estimation of the source star counts is based on the HSC photometry that is already affected by dust extinction. Hence, we do not think that dust extinction largely affects the following results.

5.3. *Expected number of PBH microlensing events*

We can now combine the estimated event rates for PBH microlensing (Section 2.2), the detection efficiency for our microlensing search of M31 cadence data (Section 5.1), and the estimated number of source stars in the M31 region (Section 5.2) to estimate the expected number of PBH microlensing events. Assuming PBHs have a single mass scale and that a fraction $\Omega_{\rm PBH}/\Omega_{\rm DM}$ of DM is made up of PBHs, we can estimate the expected number of PBH microlensing events:

$$N_{\rm exp}\left(M_{\rm PBH}, \frac{\Omega_{\rm PBH}}{\Omega_{\rm DM}}\right) = \Delta t_{\rm obs} \int {\rm d}\hat{t}\, \frac{{\rm d}\Gamma}{{\rm d}\hat{t}} \int {\rm d}m_r\, \frac{{\rm d}N_s}{{\rm d}m_r} \epsilon(\hat{t}, m_r), \tag{25}$$

where ${\rm d}N_s/{\rm d}m_r$ is the number of source stars in the apparent magnitude bin $[m_r, m_r + {\rm d}m_r]$, and $\Delta t_{\rm obs}$ is the duration of our M31 observation for which we employ $\Delta t_{\rm obs} = 6.94$ hours (corresponding to 25,000 sec). As given in Eq. (17), the differential event rate ${\rm d}\Gamma/{\rm d}\hat{t}$ depends on the PBH mass ($M_{\rm PBH}$) and the fraction $\Omega_{\rm PBH}/\Omega_{\rm DM}$. The event rate involves an integration over the distance of the lensing PBH from the Earth to a star in M31. For given mass and distance of lensing PBH, we can convert the microlensing timescale $\hat{t}$ to the FWHM timescale $t_{\rm FWHM}$. Note that the number counts ${\rm d}N/{\rm d}m_r$ and the detection efficiency ϵ are estimated in each patch of the HSC data, so we sum the expected number of microlensing events over all the patches to estimate the expected number of total events.

The expected number for the PBH microlensing events is really as high as 10^3–10^5 for M31 stars because of the combination of these numbers; the event rates per 1 hour observation time for a single star is ${\rm d}\Gamma/{\rm d}t \sim 10^{-5}$ for PBHs with $\sim 10^{-10} M_\odot$, our observation duration is 7 hours, the number of source stars is $N_s \sim 10^7$–10^9, and the detection efficiency is $\epsilon \sim 0.1$–0.8. However we found only one candidate microlensing event in our observation. We now use these results to derive an upper bound on the abundance of PBHs.

5.4. *Experimental limits on the abundance of PBHs*

We assume that the probability of finding $N_{\rm obs}$ events from our observation is given by the Poisson statistics:

$$P(k = N_{\rm obs}|N_{\rm exp}) = \frac{(N_{\rm exp})^k \exp[-N_{\rm exp}]}{k!} \tag{26}$$

where $N_{\rm exp}$ depends on the mass fraction of PBHs to DM, $\Omega_{\rm PBH}/\Omega_{\rm DM}$. Hence the 95% C.L. interval is given by

$$P(k = 0|N_{\rm exp}) \leq 0.05, \tag{27}$$

if we do not include the one remaining candidate of PBH microlensing (Fig. 13) assuming that the candidate is fake. If we assume the remaining candidate to be a real event, the interval

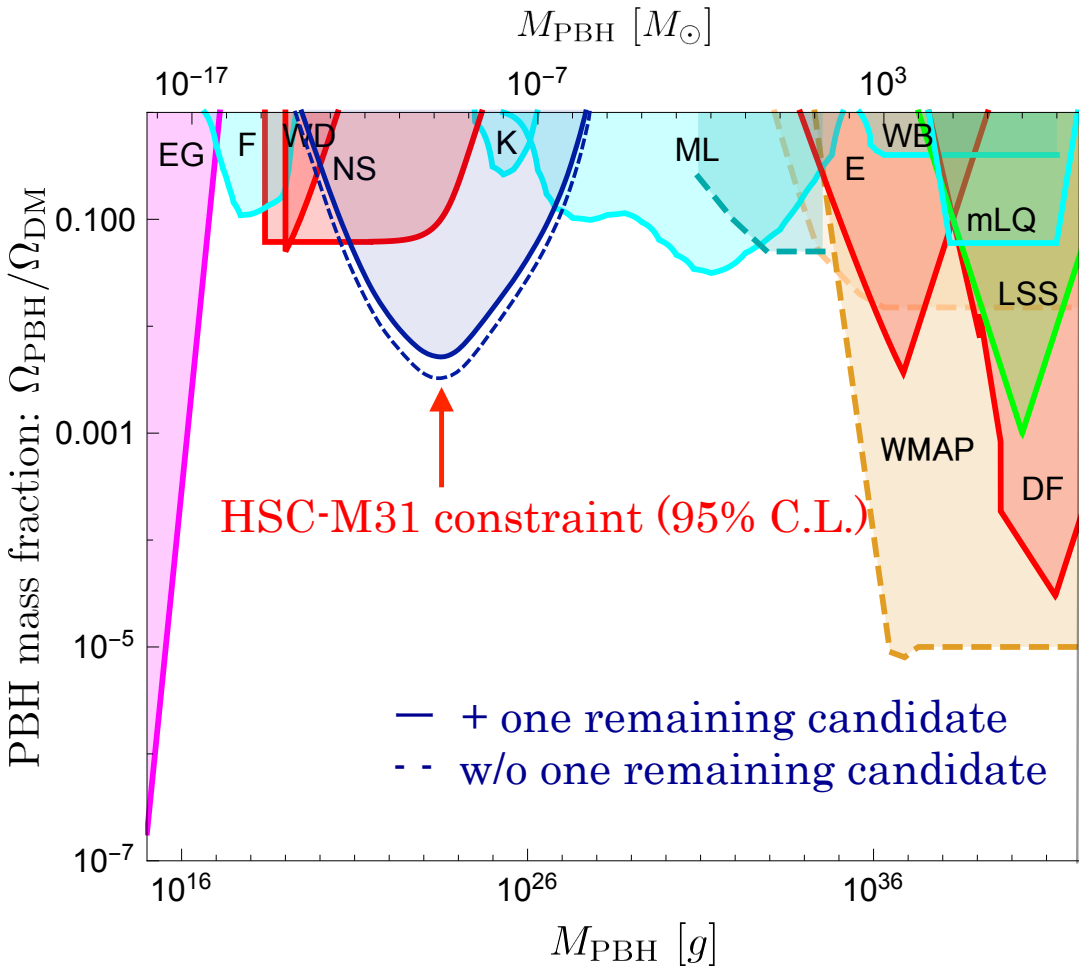

Figure 20. The 95% C.L. upper bound on the PBH mass fraction to DM in the halo regions of MW and M31, derived from our microlensing search of M31 stars with one-night HSC data, superposed on Fig. 3 in Carr et al. (2016) in order to make comparison with other constraints. The solid or dashed curves show the upper bounds if we include or exclude the one-remaining microlensing candidate in Fig. 13 in the upper bound (see Eqs. 29). For the number counts of M31 stars, we used the number of HSC peaks as a (largely) conservative estimate. Other observational constraints are: extragalactic γ-rays from PBH evaporation (EG) (Carr et al. 2010), microlensing search of stars from the satellite 2-years Kepler data (K) (Griest et al. 2014), MACHO/EROS/OGLE microlensing of stars (ML) (Tisserand et al. 2007) and quasar microlensing (overlaid dashed line) (ML) (Mediavilla et al. 2009), millilensing of quasars (mLQ) (Wilkinson et al. 2001), generation of large-scale structure through Poisson fluctuations (LSS) (Afshordi et al. 2003), and accretion effects on the CMB observables (WMAP) (Ricotti et al. 2008). The theoretically-speculated upper bounds are: white-dwarf explosions (WD) (Graham et al. 2015), neutron star capture (NS) (Capela et al. 2013), wide binary disruption (WB) (Quinn et al. 2009), survival of a star cluster in Eridanus II (E) (Brandt 2016), and dynamical friction on halo objects (DF) (Carr & Sakellariadou 1999).

becomes

$$P(k=1|N_{\rm exp}) + P(k=0|N_{\rm exp}) \leq 0.05. \quad (28)$$

These intervals read the following 95% C.L. upper limits

$$N_{\rm exp} \leq \begin{cases} 3 & \text{w/o the PBH candidate} \\ 4.74 & \text{w the PBH candidate} . \end{cases} \quad (29)$$

These translate to the upper bound on the PBH fraction, $\Omega_{\rm PBH}/\Omega_{\rm DM}$.

Fig. 20 shows our result for the upper bound on the abundance of PBH contribution to DM as a function of PBH mass, compared to other observational constraints and theoretically-speculated bounds. Here as a largely conservative estimate, we employ the number of HSC peaks for the number counts of source stars in M31, to translate the upper bounds on expected number of PBH microlensing events into a limit on the PBH abundance for each mass scale of PBH. The figure shows that our constraints are tightest for a wide range of PBH masses, $M_{\rm PBH} \simeq [10^{-13}, 10^{-6}]M_\odot$. Because of the low number of observed events, the upper bounds do not depend significantly upon our treatment of the remaining candidate (Fig. 13) as real or fake. When combined with other observational constraints labeled as "EG", "F", "K", "ML", "LSS" and "WMAP" [11], almost all the range of PBH masses is now ruled out for scenarios which result in PBHs of a single mass scale and makes up all the DM in the halo regions of MW and M31. In particular, we stress that our constraint of one-night HSC data is tighter than the constraint from the Kepler data that had monitored an open cluster containing 10^5 stars, with about 15 or 30 min cadence over 2 years (Griest et al. 2014). The constraints labeled as "WD" and "NS" are theoretically-speculated bounds in Capela et al. (2013); e.g., they discussed that the existence of neutron stars in globular clusters can be used to constrain the PBH abundance, as those can be cap-

[11] Note that the WMAP bound due to the accreting PBHs are currently under discussion, because the bound in Ricotti et al. (2008) is derived assuming too high accretion rate as discussed in Bird et al. (2016) (also see Ali-Haïmoud & Kamionkowski 2016).

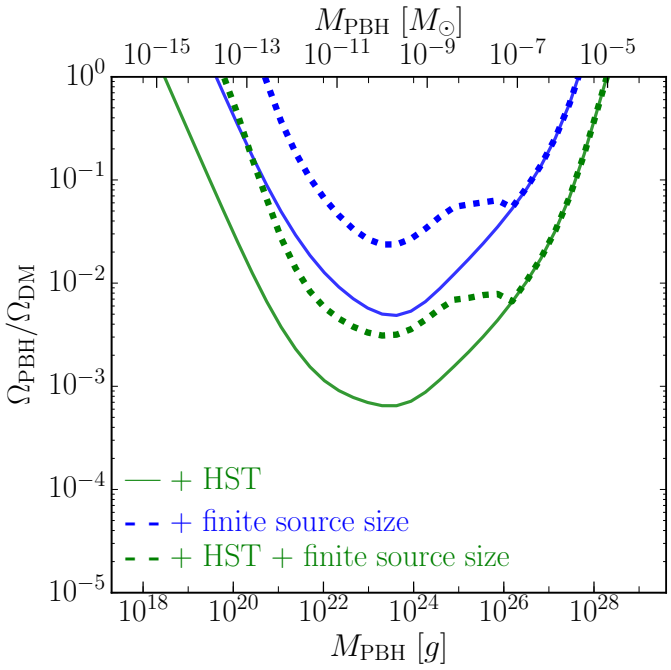
$M_{\rm PBH}\ [M_\odot]$
10^{-15} 10^{-13} 10^{-11} 10^{-9} 10^{-7} 10^{-5}
10^{0} 10^{-1} 10^{-2} 10^{-3} 10^{-4} 10^{-5}
$\Omega_{\rm PBH}/\Omega_{\rm DM}$
— + HST
- - + finite source size
- - + HST + finite source size
10^{18} 10^{20} 10^{22} 10^{24} 10^{26} 10^{28}
$M_{\rm PBH}\ [g]$

Figure 21. The green solid curve shows the 95% C.L. upper bound if we use the number counts of source stars extrapolated from the HST PHAT data (see text for the details), compared to our fiducial result using the HSC peaks (blue curve). The respective dashed curves are the results when taking into account the effects of finite source size on the event rate of microlensing (see Fig. 22), assuming a solar radius for stars in M31. The effects weaken the upper bound in the small mass range.

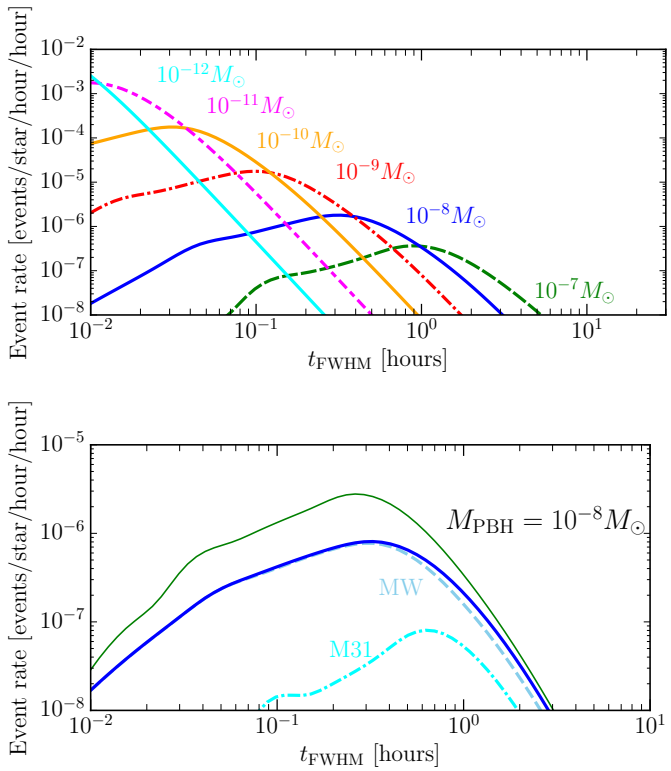

Figure 22. The event rate of PBH microlensing for a single star in M31 when taking into account the effect of finite source size. Given the fact that the HSC data (down to $r \simeq 26$ mag) is sufficiently deep to reach main-sequence stars in M31, rather than red-giant branch stars, we assume a solar radius for source star size. The finite source size effect lowers the event rate compared to Fig. 3. The lower panel shows the relative contribution of PBHs in the MW or M31 halo region to the event rate for PBHs with $M_{\rm PBh} = 10^{-8}M_\odot$. The upper thin solid curve is the result for a point source, the same as in the right panel of Fig. 3. The microlensing events in M31 are mainly from nearby PBHs to a source star at distance within a few tens of kpc (see Fig. 1), so the finite source size effect is more significant for such PBHs due to their relatively small Einstein radii.

tured by PBHs. However, observation of globular clusters show no strong evidence of significant dark matter content, so the upper bound is currently under debate. Given the disputed nature of these bounds, our results also provide the tightest constraints on mass scales $M_{\rm PBH} = [10^{-13}, 10^{-9}]M_\odot$. This shows the tremendous capability of high-cadence HSC observations of M31 in order to constrain the PBH abundance.

6. DISCUSSION

Although our results for the upper bounds in Fig. 20 are promising, we employed several assumptions. In this section, we discuss the impacts of our assumptions.

The most significant uncertainty in our bounds comes from the number counts of source stars in M31, which is a result of blending of stars in the HSC data due to overcrowding, especially in the disk regions of M31. We stress that we have used extremely conservative assumption of treating the observed number of HSC peaks as our default estimate. As discussed around Fig. 19, we can estimate the number counts of source stars in the disk regions by extrapolating the HST star counts to HSC peaks at the overlapping magnitude. In this case we have a total of about 8.7×10^7 stars, instead of 6.4×10^6 for the HSC peak counts, which gains us a factor of 14. However, the gain in number is mainly at low intrinsic fluxes, where the efficiency for microlensing detection drops precipitously. The green solid curve in Fig. 21 shows the upper bound based on using the HST-extrapolated counts of source stars. Here we have treated the one remaining candidate as a real event. The use of the HST-extrapolated counts leads to about factor of 10 tighter bound on the abundance of PBHs.

Another uncertainty in our analysis is the effect of finite source size. As can be found by comparing Eqs. (3) and (4), the angular size of the source star can be greater than the Einstein radius if PBHs are close to M31 or if PBHs are in the small mass range such of $M_{\rm PBH} \lesssim 10^{-10}M_\odot$ (assuming solar radius for the star), all of which result in a smaller Einstein radius. Compared to the distance modulus for M31 is $\mu \simeq 24.4$ mag, our HSC depth is deep enough ($r \simeq 26$ mag) to reach main sequence stars whose absolute magnitudes $M_r \simeq 1.5$ mag. According to Figures 23 and 24 in Dalcanton et al. (2012), most such faint stars at $r \sim 25$–26 mag would be either main sequence stars (probably A or F-type stars) or subgiant stars. In either case such stars have radii similar to the sun within a factor of 2 or so [12](North et al. 2007). The shallower data such as the work by de Jong et al. (2006) probes the microlensing events only for much brighter stars such as red giant branch (RGB) stars. RGB stars have much greater radius than that of main sequence stars, where the finite source size effect is more significant. Here we employ a solar radius ($R_\odot \simeq 6.96 \times 10^{10}$ cm) for all source stars for simplicity, assuming that the upper bound is mainly from the microlensing for main sequence stars, rather than for RGB stars (Dalcanton et al. 2012). We followed Witt & Mao (1994) to re-estimate the event rates of PBHs microlensing taking

[12] http://cas.sdss.org/dr4/en/proj/advanced/hr/radius1.asp

into account the finite source size effect. Fig. 22 shows that the finite source size effect lowers the event rate, compared to Fig. 3. In particular the effect is greater for PBHs of smaller mass scales and in the M31 halo region.

The dotted curves in Fig. 21 show the upper bounds when taking into account the finite source size effect, for both cases of the HSC peaks and the PHAT-extrapolated counts of source stars. As expected, the finite source size effect significantly weakens the upper bounds for PBHs of smaller mass scales. Nevertheless, our results give the tightest, observational upper bounds in the mass range, $M_{\rm PBH} \simeq [10^{-13}, 10^{-6}]M_\odot$, a range spanning 7 orders of magnitude.

7. SUMMARY AND CONCLUSION

In this paper, we have used the high-cadence data of M31, taken with the HSC/Subaru, in order to search for microlensing effects of PBHs on M31 stars. The combination of the wide field-of-view and the 8.2m aperture of HSC/Subaru is ideal for our study. The photon collecting power and the excellent image quality with 0.6″ seeing size enable us to reach main sequence stars in M31 even with a short exposure time of 90 sec. These correspond to a depth of $r \simeq 26$ mag compared to the distance modulus of M31 ($\mu \simeq 24.4$ mag). The large field-of-view enables us to cover the bulge, disk and halo regions, which contain a majority of stars in M31, with a single pointing. Our work is impossible with other telescopes of smaller aperture and narrower field-of-view. With this unique HSC data, we expect to see quite a high number for PBH microlensing events of M31 stars, if PBHs constitute a majority of DM in the MW and M31 halo regions. The event rates for a single star per one hour observation can be high up to 10^{-6}–10^{-4}, for the microlensing events that have a light curve timescale of 0.1–1 hours, which is the most sensitive window of our high-cadence data. We have about 7 hours observation duration, and we can discern up to about 10^8 total number of source stars over the HSC field-of-view. Thus, even after taking a detection efficiency that can be low as $O(0.1)$ for each event, we expected 10^3–10^4 events for our data for the PBH DM scenario.

However, the main challenge lies in the data analysis. The PBH microlensing is in the pixel lensing regime, i.e. microlensing of unresolved stars. To tackle this difficulty, we used the difference image technique in Alard & Lupton (1998), and successfully managed to find many candidate variable stars such as stellar flares, contact or eclipsing binaries, and Cepheid variables. After careful selection criteria including the microlensing fitting to the measured light curve, we concluded that most candidates are not microlensing events, but found one remaining candidate for which it is difficult to rule out the microlensing hypothesis with the currently available information (see Fig. 13). The position is (RA, dec) = (00h 45m 33.413s, +41d 07m 53.03s). If this is a real event, it is a discovery, unveiling some contribution of PBHs to DM. Alternatively the one remaining candidate could also be a result of microlensing by a free-floating planet in the halo region, rather than a PBH (Sumi et al. 2011) (again recall that the short timescale of the light curve requires a planetary mass scale, rather than stellar mass). This could also be another important discovery, especially for the halo regions, and is worth exploring. We are planning to have follow-up observations of M31 with HSC. These observations will be able to test the nature of the one remaining candidate (whether it shows a variability signature) as well as to possibly find other similar events. We could also possibly rule out scenarios which predict a wide distribution in the masses of PBHs, by significantly constraining the abundance in a wide range of mass scales.

We used these results of PBH microlensing search to derive upper bounds on the abundance of PBHs as a candidate for DM in the MW and M31 halo regions. Thanks to the high expectation number of microlensing events, our constraints are tightest for PBHs in a mass range, spanning 7 orders of magnitude, $M_{\rm PBH} \simeq [10^{-13}, 10^{-6}]M_\odot$ (see Fig. 20). We also discussed how our constraints improve by using the number counts of source stars extrapolated from the HST PHAT star catalogs in the disk region or degrade if we take into account the effect of finite source size (Fig. 21).

Our results of the HSC M31 data, together with other observational constraints, rule out almost all mass scales of PBHs, if PBHs of a single mass scale constitute all DM. More precisely, if we consider the finite source size effect, a very narrow window of PBH mass scale around $M_{\rm PBH} \simeq 10^{-14}M_\odot$ corresponding to 10^{19} g might still be allowed, if the WD/NS bounds are disputed.

Some inflation-inspired model predicts that PBHs span over a wide range of mass scales possibly extending to mass scales of a few $10M_\odot$, mass scales of the LIGO binary black holes (Kawasaki et al. 2016b,a; Inomata et al. 2016). If binary black holes for gravitational wave sources originate from PBHs, a wide mass spectrum of PBHs is required, because a scenario with $\Omega_{\rm PBH}/\Omega_{\rm DM} = 1$, for mass scales around 10 $M_\odot$, is already ruled out by observations such as MACHO microlensing and CMB constraints. Our results give a strong constraint on such a wide-mass-spectrum model; a model with $\Omega_{\rm PBH}/\Omega_{\rm DM} \gtrsim 10^{-2}$–$10^{-3}$ is not allowed for mass scales of $M_{\rm PBH} \simeq [10^{-11}, 10^{-9}]M_\odot$.

There is still some scope to improve our results. First of all, if we have more HSC nights, we can tighten the bound; e.g., if additional 10 clear nights are provided, we can tighten the upper bound by a factor of $1/\sqrt{10}$. Secondly, to extend the constraints to smaller mass scales than we did, $M_{\rm PBH} \lesssim 10^{-14}M_\odot$, we need a higher sampling rate by shortening the exposure time and/or the readout time (currently 35 sec). Since LSST allows a very short readout (2 sec) (LSST Science Collaboration et al. 2009), it can improve the constraint at the smaller mass scales, if an appropriate target for the monitoring observation such as LMC and SMC is observed with high cadence. Thirdly, we could extend our constraints to heavier mass scales, if M31 can be monitored over longer timescale from months to years. For example, if we have repeated observations of M31 every few months over 10 years, say one hour observation for each observation run, we should be able to improve the constraints at higher mass scales. Since M31 is the most suitable target in the northern hemisphere for HSC, this is a valuable opportunity, waiting to be exploited.

Our analysis involves several simplified assumptions. First, DM contents of the MW and M31 halo regions are uncertain, to within a factor of a few. In this paper, we assumed $M_{\rm vir} = 10^{12}$ and 1.6×10^{12} for halo masses of MW and M31, respectively. If these numbers were changed, the upper bounds would be changed accordingly. Secondly, the impact of finite source size effect has to be more carefully studied. In this paper, we simply employ the solar radius for all source stars, variations in source size need to be taken into account. However, these changes should be within a factor of a few, so we do not think our results are changed by a factor of 10 or

so.

ACKNOWLEDGMENTS

We would like to dedicate this paper to the memory of Prof. Arlin Crotts, a pioneer of pixel lensing. We thank Andrew Gould, Bhuvnesh Jain, Masahiro Kawasaki, Alex Kusenko, Chien-Hsiu Lee, Hitoshi Murayama, David Spergel and Masaomi Tanaka for useful discussion. This work was supported by World Premier International Research Center Initiative (WPI Initiative), MEXT, Japan, by the FIRST program "Subaru Measurements of Images and Redshifts (SuMIRe)", CSTP, Japan, Grant-in-Aid for Scientific Research from the JSPS Promotion of Science (No. 23340061 and 26610058), MEXT Grant-in-Aid for Scientific Research on Innovative Areas (No. 15H05893, 15K21733, 15H05892) and JSPS Program for Advancing Strategic International Networks to Accelerate the Circulation of Talented Researchers.

The Hyper Suprime-Cam (HSC) collaboration includes the astronomical communities of Japan and Taiwan, and Princeton University. The HSC instrumentation and software were developed by the National Astronomical Observatory of Japan (NAOJ), the Kavli Institute for the Physics and Mathematics of the Universe (Kavli IPMU), the University of Tokyo, the High Energy Accelerator Research Organization (KEK), the Academia Sinica Institute for Astronomy and Astrophysics in Taiwan (ASIAA), and Princeton University. Funding was contributed by the FIRST program from Japanese Cabinet Office, the Ministry of Education, Culture, Sports, Science and Technology (MEXT), the Japan Society for the Promotion of Science (JSPS), Japan Science and Technology Agency (JST), the Toray Science Foundation, NAOJ, Kavli IPMU, KEK, ASIAA, and Princeton University.

The Pan-STARRS1 Surveys (PS1) have been made possible through contributions of the Institute for Astronomy, the University of Hawaii, the Pan-STARRS Project Office, the Max-Planck Society and its participating institutes, the Max Planck Institute for Astronomy, Heidelberg and the Max Planck Institute for Extraterrestrial Physics, Garching, The Johns Hopkins University, Durham University, the University of Edinburgh, Queen's University Belfast, the Harvard-Smithsonian Center for Astrophysics, the Las Cumbres Observatory Global Telescope Network Incorporated, the National Central University of Taiwan, the Space Telescope Science Institute, the National Aeronautics and Space Administration under Grant No. NNX08AR22G issued through the Planetary Science Division of the NASA Science Mission Directorate, the National Science Foundation under Grant No. AST-1238877, the University of Maryland, and Eötvös Loránd University (ELTE).

This paper makes use of software developed for the Large Synoptic Survey Telescope. We thank the LSST Project for making their code available as free software at http://dm.lsstcorp.org.

REFERENCES

Abbott, B. P., et al. 2016, Physical Review Letters, 116, 061102
Afshordi, N., McDonald, P., & Spergel, D. N. 2003, ApJ, 594, L71
Alard, C. 2000, A&AS, 144, 363
Alard, C., & Lupton, R. H. 1998, ApJ, 503, 325
Alcock, C., et al. 1996, ApJ, 461, 84
—. 2000, ApJ, 542, 281
Ali-Haïmoud, Y., & Kamionkowski, M. 2016, ArXiv e-prints:1612.05644
Axelrod, T., Kantor, J., Lupton, R. H., & Pierfederici, F. 2010, in Proc. SPIE, Vol. 7740, Software and Cyberinfrastructure for Astronomy, 774015
Baillon, P., Bouquet, A., Giraud-Heraud, Y., & Kaplan, J. 1993, A&A, 277, 1
Bennett, D. P. 2005, ApJ, 633, 906
Bertin, E. 2011, in Astronomical Society of the Pacific Conference Series, Vol. 442, Astronomical Data Analysis Software and Systems XX, ed. I. N. Evans, A. Accomazzi, D. J. Mink, & A. H. Rots, 435
Bird, S., Cholis, I., Muñoz, J. B., Ali-Haïmoud, Y., Kamionkowski, M., Kovetz, E. D., Raccanelli, A., & Riess, A. G. 2016, Physical Review Letters, 116, 201301
Brandt, T. D. 2016, ApJ, 824, L31
Calchi Novati, S. 2010, General Relativity and Gravitation, 42, 2101
Calchi Novati, S., et al. 2005, A&A, 443, 911
—. 2009, ApJ, 695, 442
—. 2014, ApJ, 783, 86
Capela, F., Pshirkov, M., & Tinyakov, P. 2013, Phys. Rev. D, 87, 123524
Carr, B., Kühnel, F., & Sandstad, M. 2016, Phys. Rev. D, 94, 083504
Carr, B. J. 1975, ApJ, 201, 1
Carr, B. J., & Hawking, S. W. 1974, MNRAS, 168, 399
Carr, B. J., Kohri, K., Sendouda, Y., & Yokoyama, J. 2010, Phys. Rev. D, 81, 104019
Carr, B. J., & Sakellariadou, M. 1999, ApJ, 516, 195
Cieplak, A. M., & Griest, K. 2013, ApJ, 767, 145
Clowe, D., Bradač, M., Gonzalez, A. H., Markevitch, M., Randall, S. W., Jones, C., & Zaritsky, D. 2006, ApJ, 648, L109
Crotts, A. P. S. 1992, ApJ, 399, L43
Crotts, A. P. S., & Tomaney, A. B. 1996, ApJ, 473, L87
Dalcanton, J. J., et al. 2012, ApJS, 200, 18
Davis, M., Efstathiou, G., Frenk, C. S., & White, S. D. M. 1985, ApJ, 292, 371
de Jong, J. T. A., et al. 2006, A&A, 446, 855
Dodelson, S., & Liguori, M. 2006, Physical Review Letters, 97, 231301
Gondolo, P. 1999, ApJ, 510, L29
Gould, A. 1996, ApJ, 470, 201
Graham, P. W., Rajendran, S., & Varela, J. 2015, Phys. Rev. D, 92, 063007
Griest, K., Cieplak, A. M., & Lehner, M. J. 2014, ApJ, 786, 158
Griest, K., Lehner, M. J., Cieplak, A. M., & Jain, B. 2011, Physical Review Letters, 107, 231101
Griest, K., et al. 1991, ApJ, 372, L79
Hawking, S. 1971, MNRAS, 152, 75
Inomata, K., Kawasaki, M., Mukaida, K., Tada, Y., & Yanagida, T. T. 2016, ArXiv e-prints:1611.06130
Ivezic, Z., et al. 2008, ArXiv e-prints:0805.2366
Jungman, G., Kamionkowski, M., & Griest, K. 1996, Phys. Rep., 267, 195
Jurić, M., et al. 2015, ArXiv e-prints:1512.07914
Kawasaki, M., Kusenko, A., Tada, Y., & Yanagida, T. T. 2016a, ArXiv e-prints:1606.07631
Kawasaki, M., Mukaida, K., & Yanagida, T. T. 2016b, ArXiv e-prints:1605.04974
Kerins, E., et al. 2001, MNRAS, 323, 13
Klasen, M., Pohl, M., & Sigl, G. 2015, Progress in Particle and Nuclear Physics, 85, 1
Klypin, A., Zhao, H., & Somerville, R. S. 2002, ApJ, 573, 597
Lee, C.-H., et al. 2012, AJ, 143, 89
LSST Science Collaboration et al. 2009, ArXiv e-prints:0912.0201
Magnier, E. A., et al. 2013, ApJS, 205, 20
Mandelbaum, R., et al. 2014, ApJS, 212, 5
Mediavilla, E., et al. 2009, ApJ, 706, 1451
Miyazaki, S., et al. 2015, ApJ, 807, 22
Navarro, J. F., Frenk, C. S., & White, S. D. M. 1997, ApJ, 490, 493
North, J. R., et al. 2007, MNRAS, 380, L80
Paczynski, B. 1986, ApJ, 304, 1
Quinn, D. P., Wilkinson, M. I., Irwin, M. J., Marshall, J., Koch, A., & Belokurov, V. 2009, MNRAS, 396, L11
Ricotti, M., Ostriker, J. P., & Mack, K. J. 2008, ApJ, 680, 829
Riffeser, A., Fliri, J., Seitz, S., & Bender, R. 2006, ApJS, 163, 225
Riffeser, A., Seitz, S., & Bender, R. 2008, ApJ, 684, 1093
Roulet, E., & Mollerach, S. 1997, Phys. Rep., 279, 67
Rowe, B. T. P., et al. 2015, Astronomy and Computing, 10, 121
Rubin, V. C., Thonnard, N., & Ford, Jr., W. K. 1978, ApJ, 225, L107
Sasaki, M., Suyama, T., Tanaka, T., & Yokoyama, S. 2016, Physical Review Letters, 117, 061101
Schlafly, E. F., et al. 2012, ApJ, 756, 158
Sumi, T., et al. 2011, Nature, 473, 349
Tisserand, P., et al. 2007, A&A, 469, 387
Tonry, J. L., et al. 2012, ApJ, 750, 99
Wambsganss, J. 2006, ArXiv Astrophysics e-prints:0604278
Wilkinson, P. N., et al. 2001, Physical Review Letters, 86, 584
Williams, B. F., et al. 2014, ApJS, 215, 9
Witt, H. J., & Mao, S. 1994, ApJ, 430, 505
Wyrzykowski, Ł., et al. 2010, MNRAS, 407, 189
Zel'dovich, Y. B., & Novikov, I. D. 1967, Soviet Ast., 10, 602
Zwicky, F. 1937, ApJ, 86, 217